OBSERVATIONS OF TIDAL CURRENT AND STRATIFICATION PROFILES ON THE CONTINENTAL SHELF OUTSIDE BLOCK ISLAND SOUND

Laura Victoria Rear

B.S., The Richard Stockton College of New Jersey, 2000

A Thesis
Submitted in Partial Fulfillment of the
Requirements for the Degree of
Master of Science
at the
University of Connecticut
2002

APPROVAL PAGE

Master of Science Thesis

OBSERVATIONS OF TIDAL CURRENT AND STRATIFICATION PROFILES ON THE CONTINENTAL SHELF OUTSIDE BLOCK ISLAND SOUND

Presented by

Laura Victoria Rear, B.S.

Major Advisor ______________________________
Daniel L. Codiga

Associate Advisor ______________________________
James O'Donnell

Associate Advisor ______________________________
Christopher A. Edwards

University of Connecticut

2002

Acknowledgements

I would like to thank my advisor, Dr. Daniel Codiga, for his time and effort spent on helping me prepare for my future career in oceanography. I also would like to thank my committee members, Dr. Jim O'Donnell and Dr. Christopher Edwards, for their advice and for keeping me on track.

I owe an enormous amount of thanks to my mom, Joan, my dad, Lester, my sisters, Rachel and Vanessa, my brother, Giampaolo Buongiorno, my step-father, Jerry Kupchynsky and my great-aunt Jeannot Deuss. Even though they still think I study fish, I am grateful for their support and encouragement through the tough times.

Kristin Braidwood, my best friend in the world, has been there for me throughout this process and I thank her for every moment we have shared since freshman year of college.

My fellow classmates who started this program with me, Amy Smith, Laura Baumgartner, Safra Altman, George Waldbusser, Peter Gay, and Brett Branco and in addition, Kari Heinonen, Kim Larkin, and Carol Rosetta, offered many a shoulder to lean on and I cannot thank them enough.

I thank all of the graduate students for always being there when I needed something, especially a formula, a good laugh, or a surfing lesson.

To supplement my research I participated in educational outreach programs. These included the Taste Touch and Smell of Science overnight camp program for middle school students, run by the graduate students; Career Exploration Night for Girls, at the Norwalk Aquarium; Avery Point Day; and the Center for Talented Youth Workshop in Explorations in Marine and Ocean Sciences, at Avery Point.

I owe my sanity to Gary Buttery and the Connecticut College Concert Band; the Waterford Women's Softball Team Padget and Son's Auto; and most of all Brownie Girl Scout Troop 3330 and Daisy Girl Scout Troop 3774 and my co-leader Carlene Lange, Pleasant Valley Service Unit, Girl Scouts Connecticut Trails Council.

Finally, I would like to thank the following people at the University of Connecticut without whom the analysis for this thesis would not be possible: Todd Fake, Adam Houk, John Hamilton, Dennis Arbige, Larry Burch, Art Lima, Gary Grenier, Bob Degoursey, Dave Cohen, Jeff Godfrey, Captain Turner Cabaniss, Mate Dan Nelson and the crew of the R/V Connecticut, and the NURC ROV team.

Funding was provided by the Office of Naval Research (N00014-99-1-1020) through a National Oceanic Partnership Program grant.

TABLE OF CONTENTS

List of Tables

List of Figures

I. INTRODUCTION

The tidal current is the predominantly horizontal movement of water associated with the rise and fall of the tide. In coastal regions, tidal currents are commonly the most energetic component of the total flow. Knowledge of the horizontal and vertical structure of tidal currents is important to advance the understanding of the dispersal and net drift of suspended material in the water column, such as plankton and pollutants. It allows for better parameterization of models investigating coastal ocean circulation (Prandle, 1982a; Davies, 1992), and is a valuable resource to ocean engineers when constructing platforms and placing pipelines (Prandle, 1982a).

Shore-based high frequency radar systems such as CODAR are gaining widespread use and help capture the horizontal structure of tidal currents in the shallowest 1-2 meters. The technology is new, however, and is still being evaluated for accuracy. Furthermore, CODAR does not offer insight as to the vertical variations in tidal current amplitudes and phases in the water column, which can be substantial. *In situ* moored instruments remain necessary to investigate these flow attributes.

Prior to the last decade, observations of tidal current structure in the vertical were generally limited to measurements with low vertical resolution, for example current meters located 10’s of meters apart in the water column (e.g. Kundu et al, 1981; Maas and van Haren, 1987). Introduction of the acoustic Doppler current profiler (ADCP) has since allowed for observations of currents with vertical resolution of a few meters or less (e.g. Tsimplis, 2000). Bottom-mounted upward looking moored ADCPs generate densely sampled time-series of vertical profiles of horizontal velocity enabling detailed investigation of tidal current properties. Development of trawl resistant bottom frames (e.g., Codiga et al, 2000) facilitates this type of deployment in areas known for intense fishing activity. Current measurements investigated in this study are from such deployments, carried out as part of the Front Resolving Observational Network with Telemetry (FRONT) project. This collaborative effort between universities, government labs and private companies investigates frontal activity on the continental shelf just outside Block Island Sound, an area with complicated bathymetry in a region influenced by fresh water input from nearby coastal areas.

Observations of basic tidal current structure have been carried out all over the world. The energy of tidal currents in coastal areas differs according to water depth and location and is driven by distinct responses to astronomical forcing. For example, the semidiurnal tides M_2 and S_2 are dominant on the Camarinal Sill, Strait of Gibraltar (Tsimplis, 2000; Bruno et al., 2000), whereas on the Texas-Louisiana shelf the largest tidal current energy is in the diurnal constituent K_1 (DiMarco and Reid, 1998). At the Korea-Tsushima Strait the M_2 tidal constituent is dominant (Teague et al., 2001).

Observations of the vertical structure of tidal currents in the North Sea (Maas and vanHaren, 1987) indicate a current amplitude decrease toward the bottom of the water column and a phase advance with depth, indicating that the maximum current is reached earlier at depth than at the surface. Observations in the Celtic Sea (Soulsby, 1990) also reveal both a sharp reduction in current amplitude toward the bed and a phase advance with depth. On the Northern Grand Bank, the M_2 tidal current is nearly homogeneous in the vertical (Tang and Belliveau, 1994). Tidal currents on the Texas-Louisiana shelf show little variation in the vertical except at nearshore locations, in 20 m water depth or less, where shear is produced by bottom friction and stratification (DiMarco and Reid, 1998).

Analytic models for frictional bottom boundary layers have been developed to account for the observed amplitude decrease and phase advance (Prandle, 1982b; Maas and vanHaren, 1987). The analytic solutions determined that the structure depended on two parameters, the vertical eddy viscosity and the bed stress coefficient. At the Camarinal Sill at the Strait of Gibraltar, Tsimplis (2000) used a constant eddy viscosity model to compare with his observations and found that the model did well in describing most of the tidal current features throughout all depths.

The focus of this study is observations of tidal current and stratification profiles on the inner continental shelf outside the mouth of the Long Island Sound and Block Island Sound estuary systems (Figure 1). Fundamental observations of tidal current structure have yet to be made in this region. The contribution of tidal energy by numerous tidal constituents are examined, as is the structure of tidal currents in the horizontal and vertical. Analytic solutions applied to other sites are applied to the present site to see if observed currents are fully described by them. Influences on tidal current structure including friction, stratification, and the low-frequency flow fluctuations are investigated. For example, at other sites, variations in tidal currents are sometimes due to changing environmental conditions such as stratification (Souza and Simpson, 1996). Mean currents measured at the present study site (Figure 2) indicate that surface flow during Spring is much greater than that during Fall and Winter; variations of tidal currents during different seasons presented here appear to be related.

Section II presents the measurements and methods. Section III discusses the dominant tidal constituents at the site, and describes the observed horizontal and vertical structure of tidal currents. Hydrographic data at the site are discussed in section IV. Section V presents the analytic solution and discusses results of best-fit values of eddy viscosity and linear bed stress for near-bottom currents. Section VI investigates a time-series of current data to explore the effects of stratification, sub-tidal currents and wind on the tidal currents.

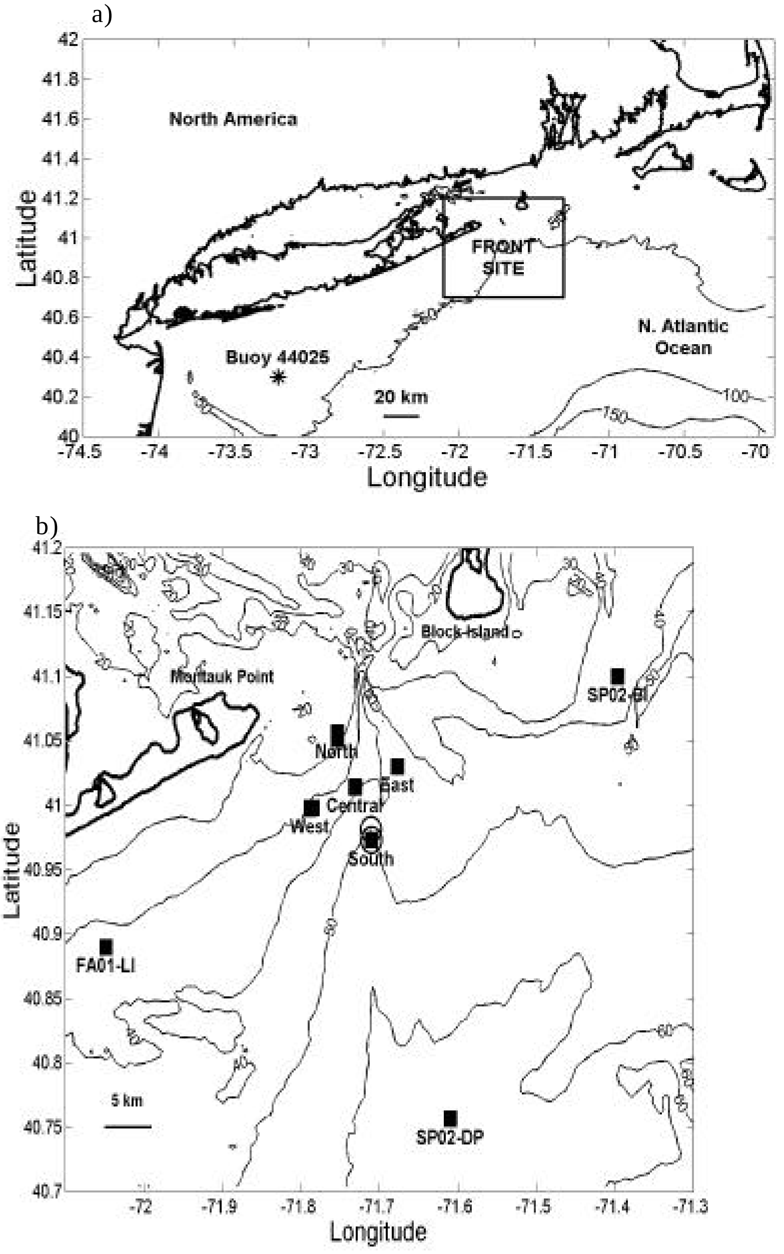

Figure 1. Field Deployment Locations a) Large scale view of study area. Contours indicate the 50, 100 and 150 m isobaths. Black box is study site. Asterisk indicates the source of wind data, Buoy 44025. b) Expanded view of boxed region in a). Bathymetry is in meters, with squares marking the ADCP deployments. Circles indicate moored CTD profiler deployments. The ADCP sites are referred to as North, Central, East, West, and South. Three deployment locations referred to in the text as far-field sites are labeled FA01-LI (Long Island), SP02-DP (Deep), and SP02-BI (Block Island).

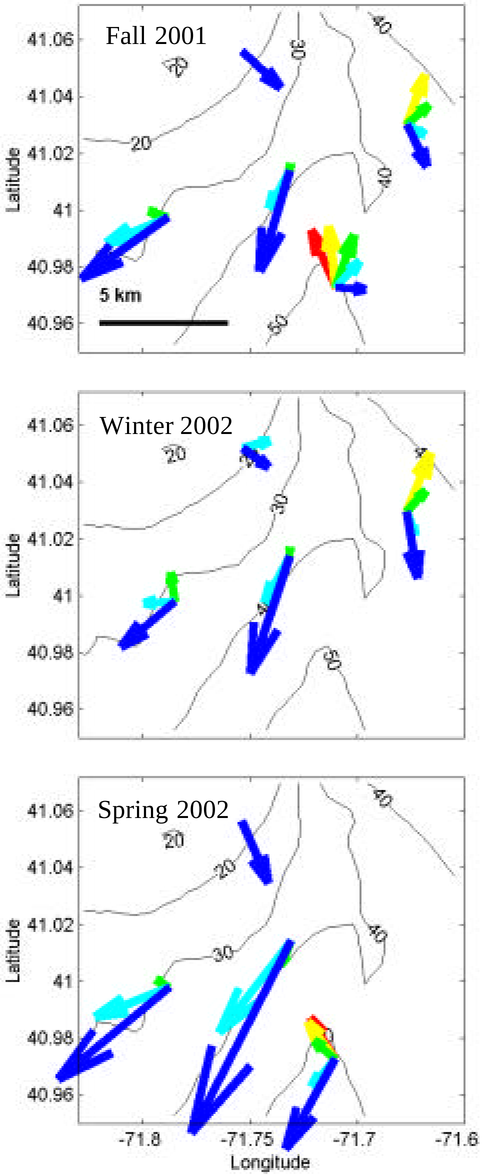

Figure 2. Mean Flow Mean flow averaged across record length (between 47 and 105 days), from Fall 2001 (top) , Winter 2002 (middle), and Spring 2002 (bottom). Vectors are 10-m depth averages centered at depths of 7, 17, 27, 37 and 47 meters, indicated by the colors blue, light blue, green, yellow, and red, respectively. The longest vector corresponds to a speed of 25 cm/s.

II. MEASUREMENTS AND METHODS

A) Study Sites and Instruments Deployed

1) ADCPs

During 1999-2002, twenty-seven upward-looking bottom-mounted RD Instruments Workhorse ADCPs were deployed on the inner continental shelf outside of Block Island Sound in 20-70 meters water depth (Codiga and Houk, 2002; available at the web address http://www.nopp.uconn.edu/ADCP/index.html). Sixteen ADCP records from the above twenty-seven are used in this study; their duration, locations, depths, and bin sizes are given in Table 1. In the Fall 2001, Winter 2002 and Spring 2002, a central array of ADCPs consisted of five sites referred to as North, South, East, West and Central, according to their locations in the array (Figure 1). In addition to the central array, one ADCP was deployed at each of the following locations referred to as the far-field sites (Figure 1): 20 km southwest of the FRONT site off Long Island (FA01-LI), 20 km northeast of the site off Block Island (SP02-BI), and 20 km south of the FRONT site, the deepest site (SP02-DP). Instrument frames at the South site in Winter 2002 and at the East site in Spring 2002 showed evidence of trawling impacts and their ADCPs returned only a few days of good data that was inadequate to include in the present analysis.

Deployment name	Startday yy/mm/dd	Endday yy/mm/dd	Lon deg W	Lat deg N	z_{wat} m	z_{min} m	z_{max} m	Bin m
SP01-C	01/03/12	01/05/27	71.71	40.98	46.9	4.4	43.7	0.96
FA01-LI	01/09/04	01/11/15	72.05	40.89	32.7	3.3	29.3	1
FA01-W	01/09/04	02/03/09	71.79	41.00	32.9	3.1	30.6	0.5
FA01-S	01/10/02	01/12/11	71.71	40.97	54.7	5.3	51.3	1
FA01-N	01/10/02	02/01/15	71.75	41.06	14.6	1.8	12.3	0.5
FA01-E	01/10/02	02/03/12	71.68	41.03	48.7	5.3	45.3	1
FA01-C	01/10/03	02/01/14	71.73	41.01	36.7	4.3	33.3	1
WI02-N	02/01/14	02/03/05	71.75	41.05	17.2	1.2	14.2	0.5
WI02-E	02/01/14	02/03/07	71.68	41.03	48.6	4.3	45.3	1
WI02-W	02/01/17	02/03/12	71.79	41.00	33.1	2.9	31.4	0.5
WI02-C	02/01/22	02/03/10	71.73	41.01	36.7	4.3	33.3	1
SP02-N	02/03/21	02/06/04	71.75	41.06	14.3	2.1	12.1	0.5
SP02-C	02/03/21	02/06/03	71.73	41.01	36.5	4.2	33.2	1
SP02-W	02/03/21	02/06/03	71.79	41.00	32.6	3.3	30.8	0.5
SP02-S	02/03/21	02/06/03	71.71	40.97	54.6	5.3	51.3	1
SP02-DP	02/03/21	02/06/04	71.61	40.76	66.3	6	63	1
SP02-BI	02/04/19	02/06/04	71.40	41.10	38.4	4.1	35.1	1

Table 1. Information about the ADCP Deployments. Column headings refer to the deployment name (given as FA01, WI02, or SP02 with suffix corresponding to location on the map in Fig 1., beginning and end dates, latitude and longitude, water depth ('z_{wat}'), the center depths of the shallowest ('z_{min}') and deepest ('z_{max}') vertical bins, and the vertical bin size. The time interval between ensembles for all records was 20 minutes except at WI02-C where it was 80 minutes. Instruments operate at 300 kHz, except at FA01-W, FA01-N, WI02-W, SP02-N, and SP02-W where they were at 600 kHz. Standard error due to instrumental uncertainty is less than 2 cm/s.

2) Moored CTD Profilers

Conductivity, temperature and pressure (CTD) profiles were obtained in addition to velocities, using moored CTD profilers (Ocean Sensors 500 Autonomous Profiling Vehicle model). Two deployments returned useful data records of at least three weeks duration; others were disrupted presumably by fishing activity. One profiler record spans 21 days in May 2001, referred to here as "Spring 2001", while the second record spans 24 days in October 2001, referred to as "Fall 2001". The Spring 2001 and Fall 2001 sites are within 1 km of each other near the South ADCP site (see Figure 1b), and in 47 and 55 meters water depth, respectively. Each was co-located with an ADCP. The CTD mooring consists of an anchored wire held taut with flotation 1-2 meters below the water surface. The profiler moves up and down the wire on rollers. The buoyancy of the instrument is controlled by a piston that is either extended (buoyancy excess) or retracted (buoyancy deficit) and causes the profiler to move up or down respectively. The instruments were programmed to profile the water column at a 2-hr interval.

B) Data Reduction and Analysis Methods

1) Currents

Data from the deepest ADCP bin, and from bins greater than 94% of the water depth from the sea floor, are considered contaminated and are omitted from the analysis (RDI, 1998). Given that the complexity of the bathymetry at the site offers little justification to rotate the coordinates to along- and across- isobath coordinates, the analysis is carried out in terms of the velocity components u (positive east), and v (positive north).

Tidal harmonics have amplitudes (A^u and A^v), phases (ϕ^u and ϕ^v) and frequencies, ω, expressed

$$u = \mathrm{Re}\{\tilde{u}\exp(i\omega t)\} = A^u\cos(\omega t - \phi^u) = A\cos\omega t + B\sin\omega t \qquad (1)$$

$$v = \mathrm{Re}\{\tilde{v}\exp(i\omega t)\} = A^v\cos(\omega t - \phi^v) = C\cos\omega t + D\sin\omega t\ . \qquad (2)$$

Here, $\tilde{u} = A^u\exp(-i\phi^u)$ and $\tilde{v} = A^v\exp(-i\phi^v)$ are complex amplitudes and A and C are the east and north cosine coefficients while B and D are the east and north sine coefficients. Following Prandle (1982b), Maas and Van Haren (1987) and Visser (1994) the complex velocity $\tilde{R} = u + iv$, is defined in terms of counter-clockwise, U^+, and clockwise, U^{-*}, complex amplitudes as

$$\tilde{R} = U^+\exp(i\omega t) + U^{-*}\exp(-i\omega t)\ , \qquad (3)$$

where the asterisk indicates the complex conjugate. The complex amplitudes can be written $U^+ = A^+\exp(i\phi^+)$ and $U^- = A^-\exp(i\phi^-)$, where $A^\pm$ and $\phi^\pm$ represent real counter-clockwise (+) and clockwise (-) amplitudes and phases.

The counter-rotating complex amplitudes add to form a tidal current ellipse (Figure 3; see Godin, 1972). Tidal current ellipse attributes can be represented by four parameters: the semi-major axis or maximum current velocity (L_{maj}, a positive quantity), the semi-minor axis (L_{min}), the inclination (Θ) or the angle that the semi-major axis makes with east, measured counter-clockwise, and the phase angle (Φ), where Φ/ω is the time at which the current is directed along the semi-major axis. In terms of the above quantities, the ellipse parameters can be written

$$L_{maj} = A^+ + A^-, \tag{4}$$

$$L_{min} = A^+ - A^-,$$

$$\Theta = 1/2\ (\phi^+ + \phi^-), \text{ and}$$

$$\Phi = 1/2(\phi^- - \phi^+).$$

A fifth parameter, the eccentricity, is defined as $\varepsilon = L_{min}/ L_{maj}$ and varies between -1 and +1, depending only on the sign of L_{min}. If ε is positive ($L_{min} > 0$) the velocity vectors trace the tidal ellipse in a counterclockwise direction, and if ε is negative ($L_{min} < 0$) the ellipse is traced clockwise.

Velocity observations at each depth were used to compute the semi-major axis, semi-minor axis, inclination, and Greenwich phase based on Godin's (1972) least-squares method, as implemented by Pawlowicz et al. (2002). The Greenwich phase lag for a given constituent is the phase lag of the maximum current along the Northward major axis with respect to the time of maximum equilibrium tide at Greenwich, England. In this study, all Greenwich phase lag results are presented by current ellipses plotted with instantaneous vectors at the time of maximum equilibrium tide at Greenwich (Figure 3). A positive Greenwich phase lag means that the instantaneous vector has not yet reached alignment with the Northward major axis.

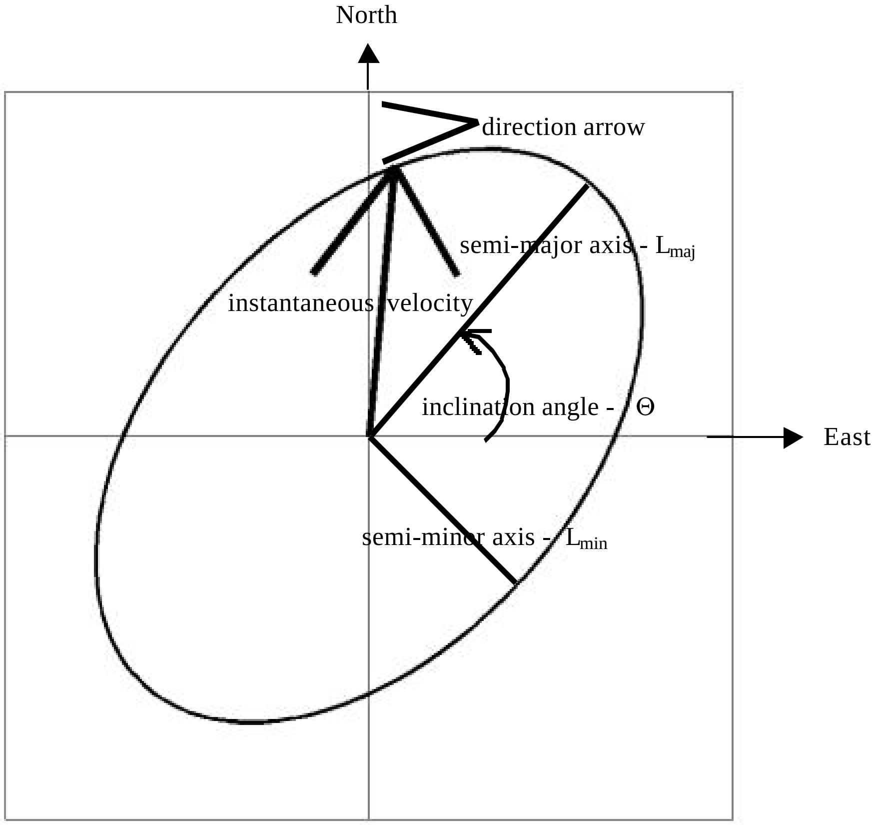

Figure 3. Tidal Ellipse Components The tidal ellipse is shown in plan view with semi-major and semi-minor axes labeled. The inclination angle Θ is the angle that the semi-major axis makes with the east direction. The instantaneous velocity is shown with direction arrow near its head indicating the direction of its rotation with time. In this example the velocity vector rotates clockwise with time, tracing out the ellipse with its tip in the course of one tidal period. The instantaneous vector is plotted using Greenwich phase lag, the phase lag of the maximum current along the Northward major axis with respect to the time of maximum equilibrium tide at Greenwich, England.

Pawlowicz et al.'s (2002) tidal package resolves specified tidal constituents and accounts for nodal corrections, which are slow changes in amplitude and phase of major tidal constituents caused by the effect of all the surrounding constituents. Inference corrections are made for those constituents whose frequency resolution is not readily resolved by using a known relationship between surrounding constituents.

Error estimates in the calculated tidal ellipse parameters (95% confidence intervals) are calculated using a bootstrapping technique.

Five tidal constituents used in the analysis, O_1, K_1, N_2, M_2, S_2, are calculated to be the most energetic based on harmonic fits to the vertical mean ADCP currents using 69 astronomical and shallow water tidal constituents. These tidal constituents and their associated periods are O_1, the principal lunar diurnal declination, 25.82 hours; K_1, the lunisolar diurnal declination, 23.94 hours; N_2, the larger lunar elliptic semidiurnal component, 12.66 hours; M_2, the principal lunar semidiurnal, 12.42 hours; and S_2, the principal solar semidiurnal, 12.00 hours (e.g. Knauss, 1997).

The ratio, V_E, of the variance, s^2_{KE} , of the kinetic energy per unit mass, $KE = 1/2\ (u^2 + v^2)$, of the tidal fit to that of the measured flow was calculated using

$$V_E = \frac{s^2_{KE_{fit}}}{s^2_{KE_{dat}}} \text{ x } 100. \tag{5}$$

Here the subscript "fit" refers to the multi-constituent harmonic fit and "dat" refers to the total measured velocity. The percent energy explained by each tidal constituent is defined

$$E_n = \frac{KE_n}{\sum_{i=1}^{N} KE_i} \text{ x } 100 \tag{6}$$

where $KE_n = 1/2(u_n^2 + v_n^2) = A_n^2 + B_n^2 + C_n^2 + D_n^2$, and n is an index of the N tidal constituents in the harmonic fit (e.g., for N = 5, n = 1,2,3,4,5 corresponding to O_1, K_1, N_2, M_2, S_2).

2) Hydrography

Conductivity, temperature and pressure values measured nominally each several centimeters in the vertical were averaged in 1 meter bins. Density anomaly sigma-t (σ_t) and the buoyancy frequency squared

$$N^2 = -(\frac{g}{\rho})(\frac{d\sigma_t}{dz}), \qquad (7)$$

with ρ a constant mean background density, were calculated using Matlab-based equation of state utility routines by Phil Morgan (available at the web address http://www.marine.csiro.au/~morgan/seawater/).

3) Winds and Tidal Heights

Wind speeds are from the National Data Buoy Center buoy 44025 located at 40.3° N latitude and 73.2° W longitude (see Figure 1a). Wind stress is calculated using the method of Large and Pond (1981). A 25-hour half-width triangle low-pass filter was applied to the record and it was subsampled to 5 hour intervals. Hourly tidal height data are from Montauk Point Fort Pond Bay, obtained from the National Oceanic and Atmospheric Administration website (http://www.co-ops.nos.noaa.gov).

III. Tidal Currents

In this and the following two sections, tidal current characteristics are described based on calculations using full-length ADCP records (between 46 and 105 days duration). Fluctuations of tidal current attributes on shorter time scales are discussed in Section VI.

A. Energy Partition

The kinetic energy variance (V_E) explained by the fit of the vertical-mean ADCP currents to the five tidal harmonics (O_1, K_1, N_2, M_2, S_2) varies with water depth, site location and season (Figure 4, pie charts). The range of values is 47-95%, with an average of 66%. At shallower inshore sites (e.g. North), the currents are in general more tidal than at deeper sites and sites farther offshore. The far-field sites are only 25-35% tidal. This distribution of tidal energy is due to the strong tidal response of Long Island and Block Island Sounds; similar results are reported for horizontal tidal energy distribution on the Texas-Louisiana shelf (DiMarco and Reid, 1998).

The semidiurnal constituent M_2 is dominant at all sites with percent energy (E_n) of 85- 90% for five-constituent fits (Figure 4, bargraphs). The other four constituents account for less than 10% each of the total summed kinetic energy, with N_2 being the next most important. A relatively energetic N_2 component observed is similar to that seen in the lower Chesapeake Bay where N_2 dominates S_2 causing primary and secondary consecutive spring-neap cycles (Valle-Levinson et al., 1998).

At the far-field sites, the percent energy (E_n) in M_2 is slightly lower, while that of the other four constituents increases, particularly the relative amounts of O_1 and K_1. This change in energy is most likely due to the selective resonance of the LIS/BIS system, for which the natural period better matches semidiurnal constituents than diurnal.

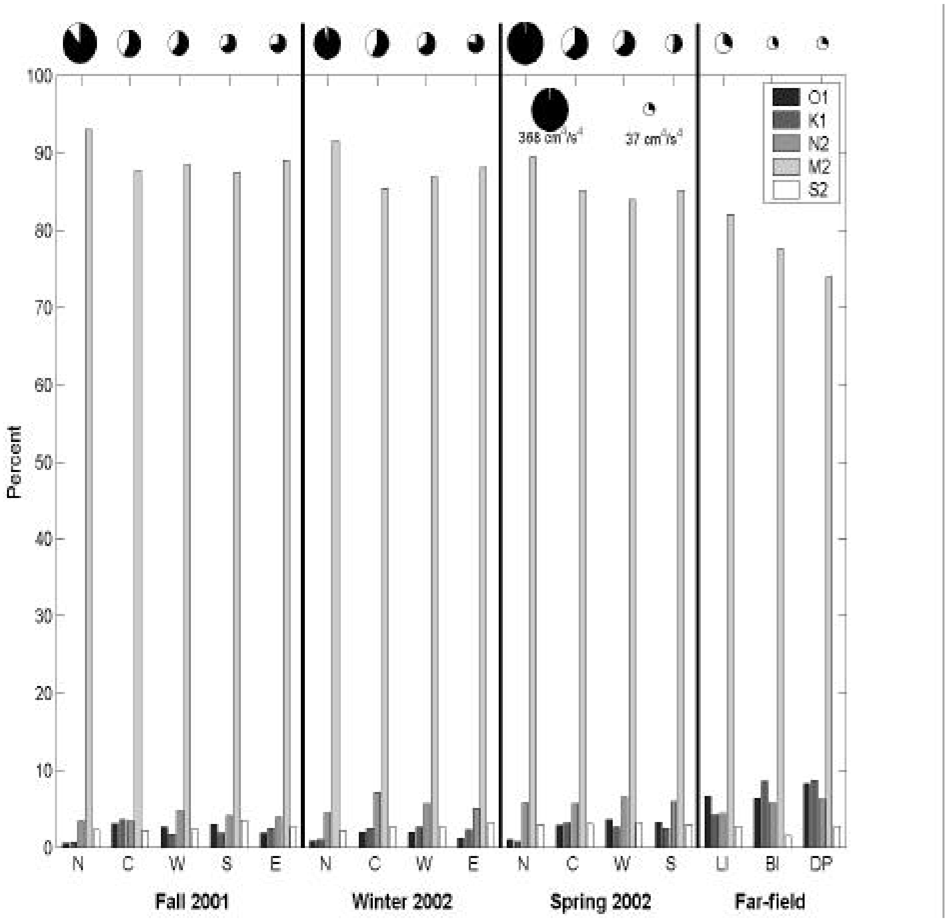

Figure 4. Kinetic Energy Partition Pie charts indicate the portion of the energy that is tidal (black) vs nontidal (white) and have area scaled proportional to the maximum total kinetic energy variance; labeled pies provide maximum and minimum values of total (summed tidal and nontidal) kinetic energy variance. Each set of five bars indicates the percent tidal energy (E_n) in the vertical mean currents for each of the 16 deployments.

To test the sensitivity of these results to inclusion of 5 constituents, fits were re-calculated using the 8 most energetic constituents as well as the 3 most energetic tidal constituents. For the 8-constituent tidal fit, the next 3 most energetic constituents $2Q_1$, NO_1, and L_2, were added; for the 3-constituent fit, O_1 and S_2 were removed. The kinetic energy variance (V_E) explained by the 8-constituent fit changes by ± 3% from that of the 5-constituent fit. M_2 is still dominant and the percent energy (E) changes by - 1% at most. The 3 added constituents each account for less than 1% of the energy. The kinetic energy variance (V_E) explained by the 3-constituent fit changes by as much as -14% from that of the 5-constituent fit. Dominance by M_2 remains, but with higher percent energy (~93%) than when 5 or 8 constituents are used, simply because the total must sum to 100%. Use of 5 tidal constituents is considered adequate, as additional constituents do not alter any of the conclusions drawn here. The remainder of the study focuses on the dominant semi-diurnal constituent M_2.

B. Horizontal Structure

The vertical-mean M_2 tidal currents (Figure 5) decrease substantially in amplitude in the offshore direction. Ellipse major axes (L_{maj}) fall from 55 cm/s at the North site to 20 cm/s at the South site. These correspond to nominal tidal advection lengths, L_{maj}/ω, of 3.9 km and 1.4 km respectively. Ellipses are traced in the clockwise direction and are oriented with major axes directed towards the mouth of

Block Island Sound. Ellipse major axes are oriented across or along isobaths to point in the direction of the estuary mouth, indicating that the complex local bathymetry plays a relatively minor role in determining ellipse orientation.

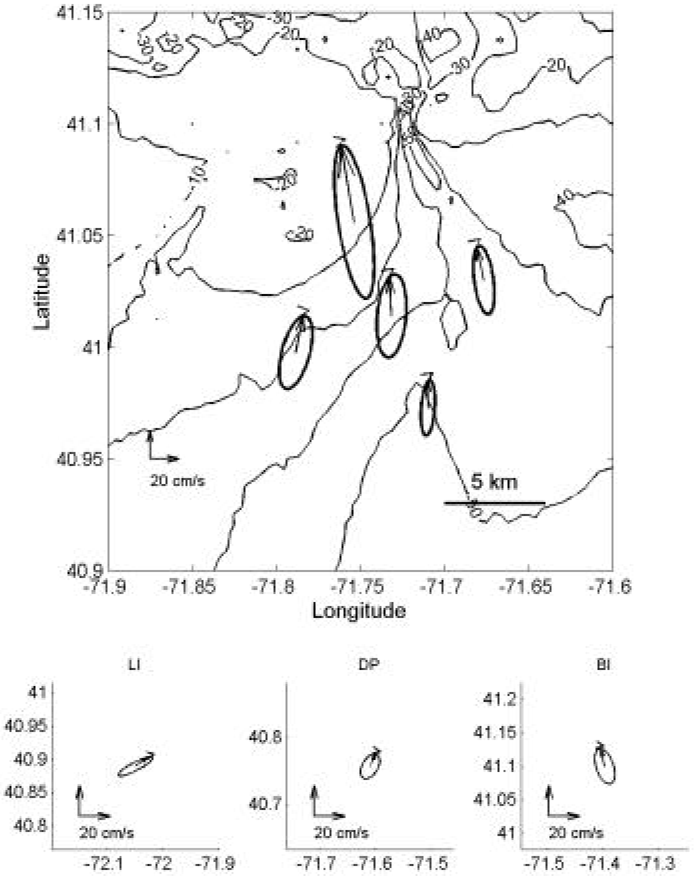

Figure 5. Vertical-mean M_2 Tidal Ellipses. Vertical-mean M_2 tidal ellipses (Figure 3) are shown for the central array in Fall 2001. The ellipse size on the plot accurately represents the distance by which a water parcel would move if subjected to tidal advection only. Isobaths are in 10-m intervals. Lower three boxes show vertical-mean M_2 tidal ellipses from the far-field sites, LI, DP, and BI (see Figure 1a for corresponding locations).

The three far-field sites have moderately weaker amplitudes (~8 cm/s). Tidal ellipses to the south of Long Island (FA01-LI) are directed along the shore with an inclination of ~30°. Off Block Island, (SP02-BI) ellipses are directed to the East of the island (Θ = 110°) and the instantaneous velocity reveals a phase advance relative to the central array. At the deeper offshore site (SP02-DP) the ellipses are nearly circular in shape and have an inclination angle of 60°.

C. Vertical Structure

Several general characteristics of the vertical profiles of tidal current ellipses are observed during all three seasons (Figures 6, 7, 8). Ellipses are traversed in a clockwise direction throughout the water column. In the deepest 5-15 meters, as the bottom is approached there is a decrease in current amplitude by about 10-15 cm/s, ellipse inclination decreases by 20-50º, and there is a phase advance in the range of 10-50º, indicating that the time of maximum current near the bed precedes that near the surface.

Differences among seasons are observed as well. At the Fall 2001 South and East sites, ellipses at depth are degenerate (rectilinear), unlike in other seasons. In the Fall 2001, current amplitude is relatively uniform with depth throughout the upper water column, then decreases with increasing depth. In contrast, during Spring 2002 a more pronounced mid-depth maximum occurs at most sites (Figure 8). These seasonal differences are explored in the next subsection.

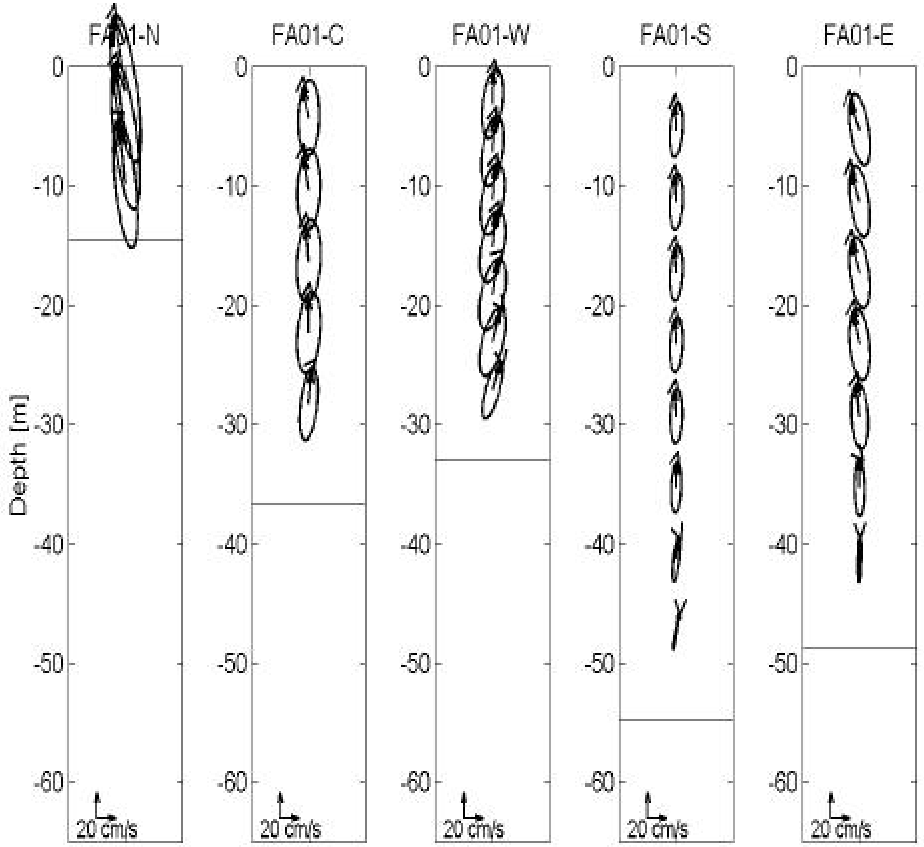

Figure 6. Ellipse Variations with Depth for Fall 2001 Ellipses at the North, Central, West, South and East sites. The horizontal line indicates water depth.

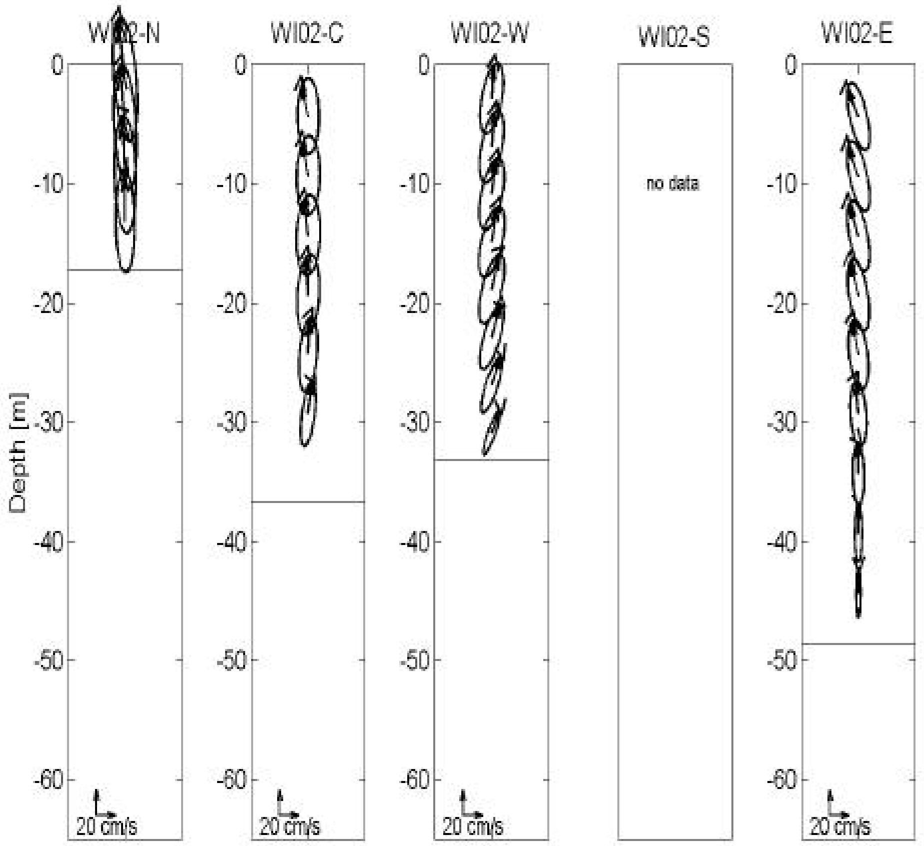

Figure 7. Ellipse Variations with Depth for Winter 2002 As in Figure 6, for Winter 2002. Note the South site is missing.

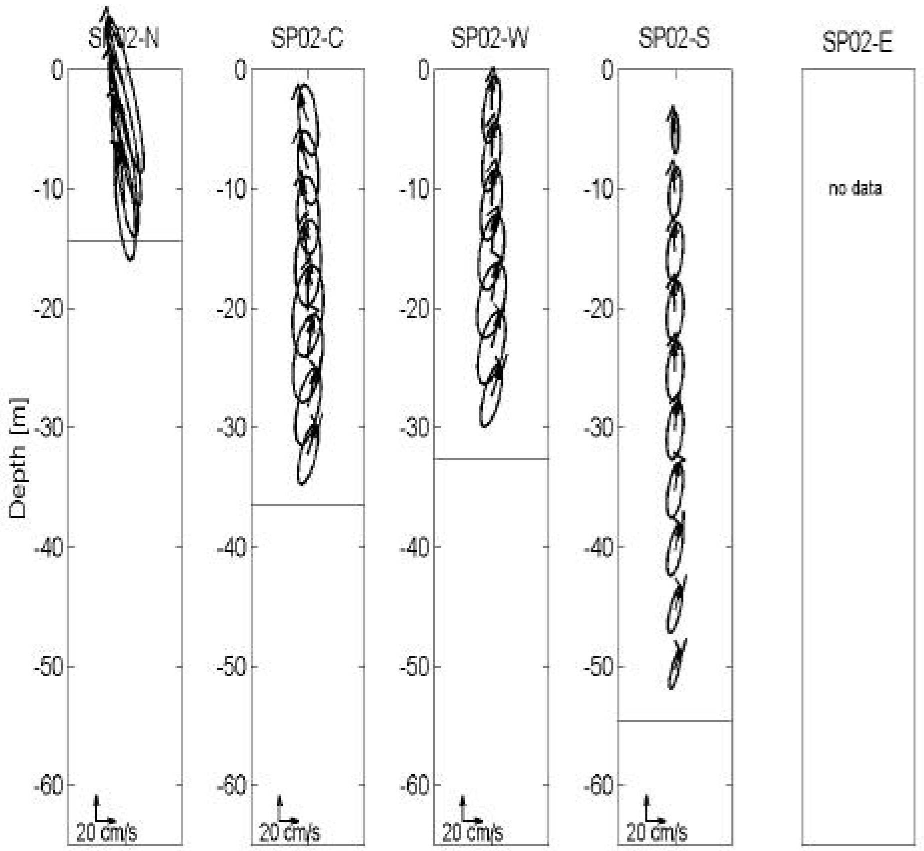

Figure 8. Ellipse Variations with Depth for Spring 2002 As in Figure 6, for Spring 2002. Note the East site is missing.

The far-field ellipses (Figure 9) at FA01-LI, like those at the central array, have amplitudes that decrease and a phase that advances with increasing depth. At the SP02-BI site a mid-depth maximum in amplitude is also observed. In contrast, ellipses at the deep site (SP02-DP, third frame Figure 9) have very little vertical structure, which can be attributed to the lessened frictional influence due to their lower amplitude.

Profiles of the four ellipse parameters, for example at the South site in Fall 2001 (Figure 10, upper row), are an alternative way to present current ellipse attributes including 95% confidence intervals. Confidence intervals are smaller than the variations of parameters with depth discussed above. The clockwise (CW) and counter-clockwise (CCW) rotating amplitudes and phases (Figure 10, lower row) indicate that the CW component is larger than the CCW component.

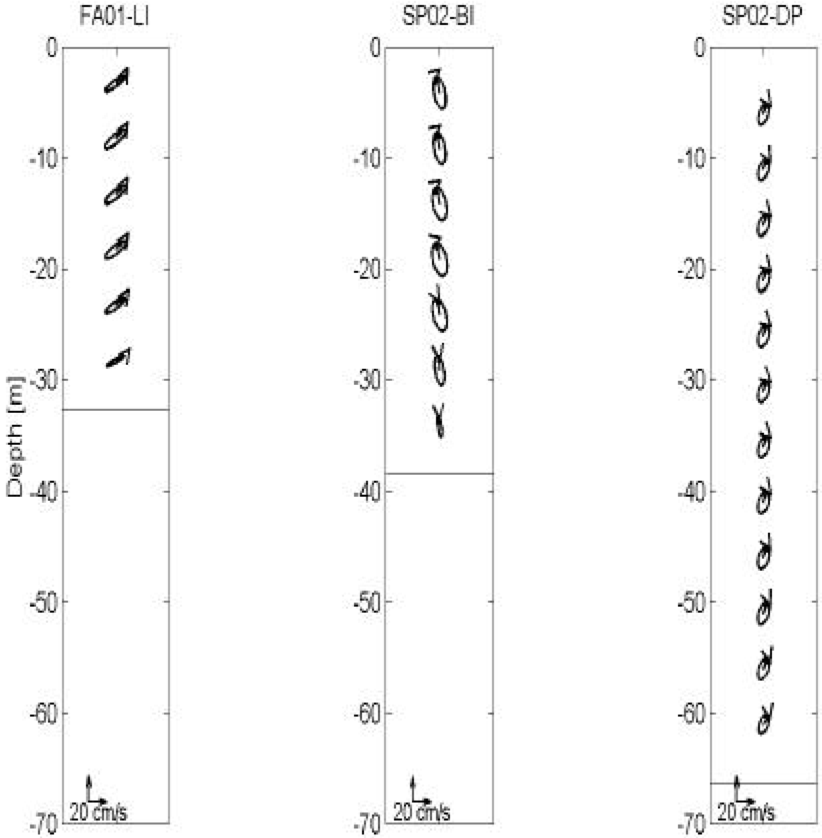

Figure 9. Ellipse Variations with Depth at Far-field Sites Ellipses for Long Island, Block Island and Deep far-field sites. Shown as in figure 6.

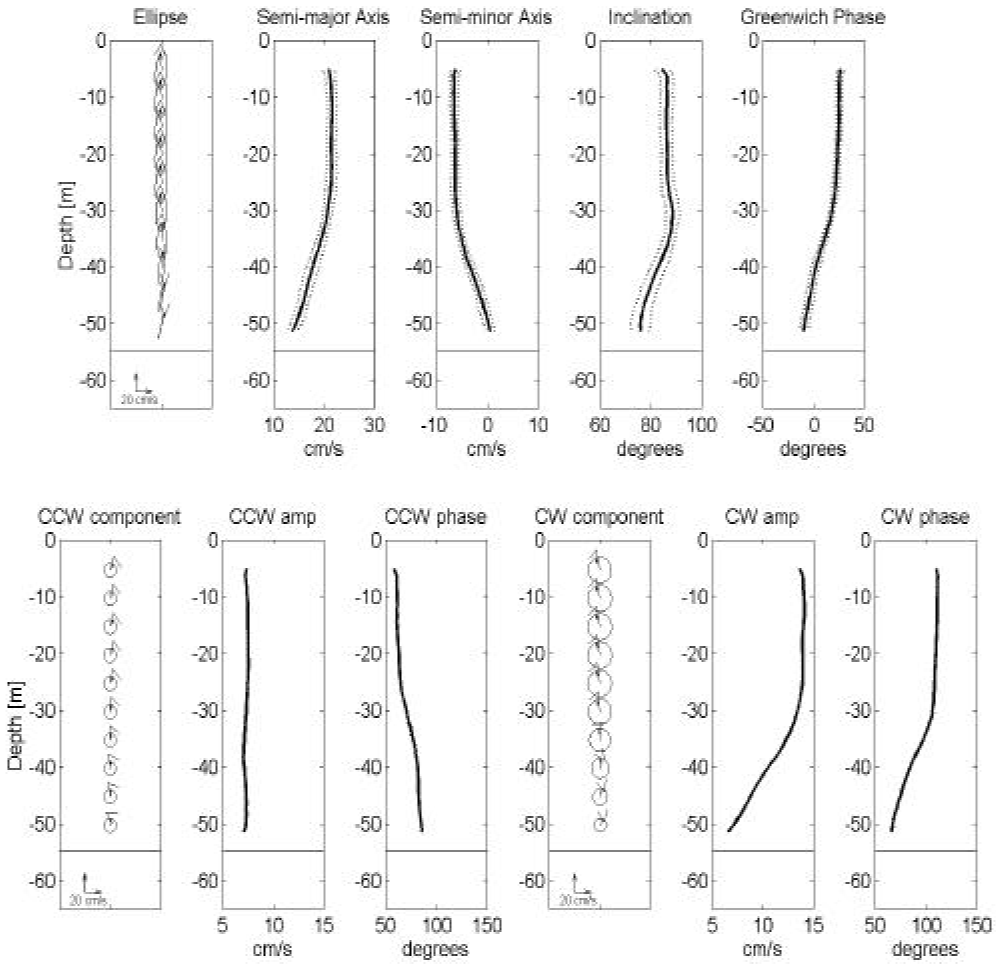

Figure 10. Ellipse Parameters and CW/CCW Components Upper row: Tidal current ellipses (left) and corresponding ellipse parameters (right) with 95% confidence intervals. Lower row: Decomposition of ellipse into CCW and CW components.

D. Differences in Vertical Structure between Spring and Fall

The differences between vertical structure of tidal current ellipses during Spring and Fall periods described in the previous subsection suggest that seasonal shifts in stratification may be responsible. In this section this possibility is explored. To do so, two ADCP records from nearly the same location, one from Spring 2001 and one from Fall 2001, are compared (SP01-C and FA01-S, see table 1). These two records are the focus because during each a moored CTD profiler collected density profiles (described in more detail in Section IV) for about a one-month subset of its length.

There are substantial differences in the vertical structure of the tidal current ellipses between the Fall and Spring (Figure 11). In the Fall, the ellipses are oriented with their major axes roughly northward (inclination angle ~85°) and are nearly uniform in the vertical throughout the upper water column. In the Spring, the ellipses have trends similar to those in the Fall in the deeper part of the water column, but in the shallowest ~15 m they deviate strongly: the amplitudes increase to about one and half times greater than Fall surface values, and the major axis is oriented roughly northwestward (inclination angles of ~95°). These qualitative characteristics of the Spring current ellipses are also apparent in more than one of the Spring 2002 records (Figure 8), which suggests they may occur each Spring.

The record-mean density anomaly (sigma-t) profiles from the month-long time-series of moored CTD profiler measurements also differ appreciably between the Fall and Spring (Figure 11, last column), although their top-to-bottom sigma-t differences are similar. In the Fall, there is a two-layer structure with the upper and lower water column nearly uniform in sigma-t and separated by a relatively sharp interface. In the Spring, the lower layer is similarly uniform in sigma-t but the interface is not a sharp step, rather a density anomaly gradient that is more uniform in depth occupies the entire upper layer. In both seasons, the structure seen in vertical profiles of current ellipse parameters appears to occur at depths aligned with changes in the sigma-t profile.

While it is likely that the different Fall and Spring stratification profiles play a role in the differences in tidal current ellipses, the record-mean currents (Figure 11, sixth column) during the two records indicate that they might play a larger role than the stratification. The surface mean flow in Spring (~ 25 cm/s) is much larger than that of Fall (~5 cm/s) (Figure 2). The larger mean flow extends to a depth of 20 meters, which matches the depth penetration of the maximum deviation between Spring and Fall tidal ellipse parameters.

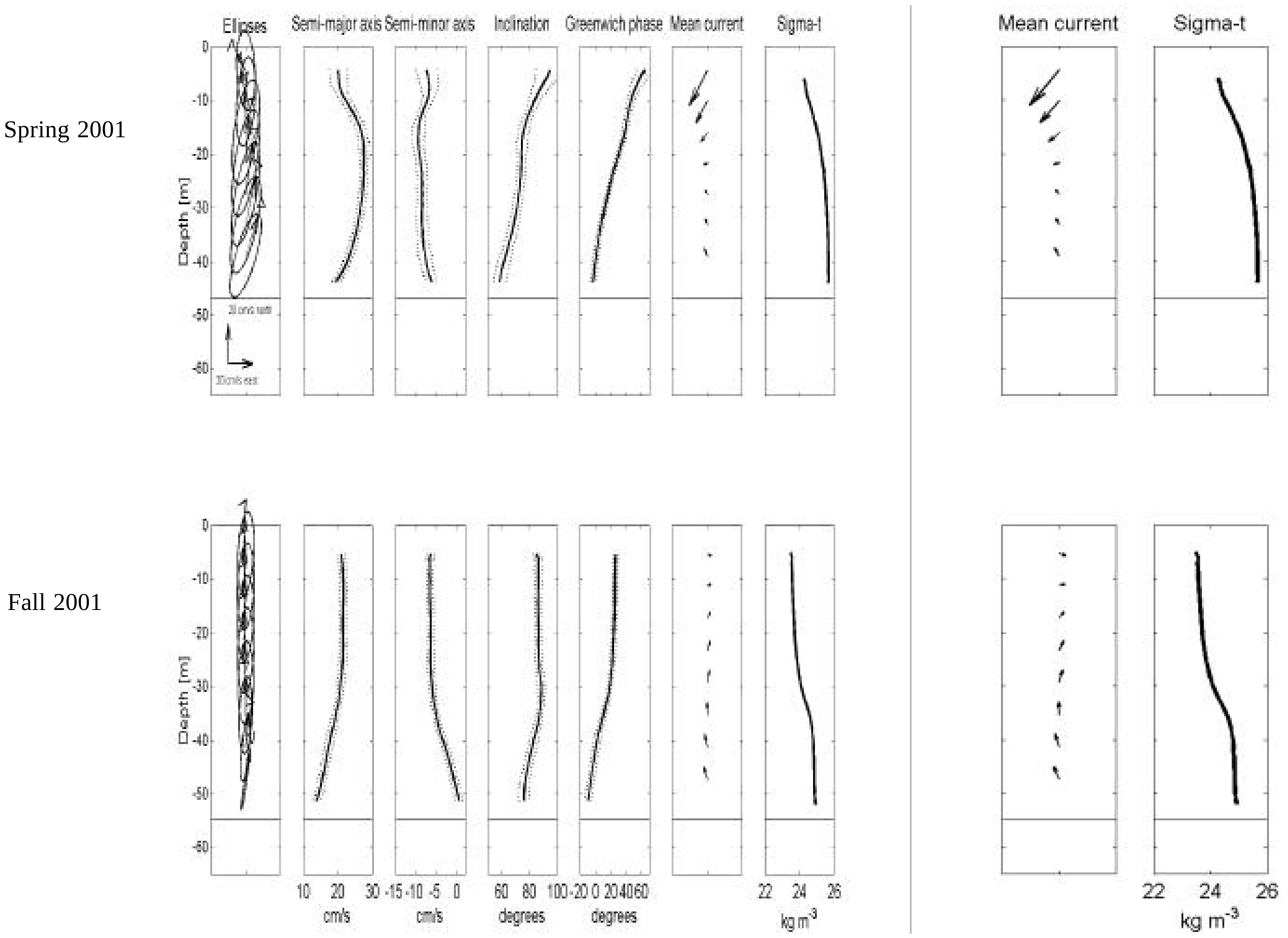

Figure 11. Ellipse Parameters with Mean Flow and Sigma-t Tidal ellipses and ellipse parameters, with mean flow and mean density anomaly profile, for Spring 2001 (top) and Fall 2001 (bottom).

IV. Stratification Profile Time-series

A. Record-mean Profiles

Moored CTD profilers returned useful data for a little less than a month each in Spring 2001 and Fall 2001. During both deployments, the temperature and the salinity act to stabilize the density.

In Spring 2001 (Figure 12), the density anomaly (sigma-t) of the water was 24 kg/m^3 in the upper 10 meters of the water column and increased to 25.5 kg/m^3 at a depth of 30 meters. Below 30 meters, the water column was homogeneous with a sigma-t of ~ 26 kg/m^3. Warmer water (10° C) persisted at depths above 25 meters; below this depth water was 6° C. Less saline water (practical salinity of 31) was located near the surface, whereas practical salinities of 32.5 were found at depth.

In Fall 2001, (Figure 13), the density anomaly of the water above 35 meters ranged from 23.5 to 24 kg/m^3, and below this depth it was roughly 25 kg/m^3. The temperature above 35 meters ranged from 16-18° C and below that depth water was colder (11-13° C). The practical salinity above 35 meters was 32.5 and at depth it was higher (~ 34).

The record-mean sigma-t profiles (Figure 14) reveal that in Spring 2001 the density anomaly near the surface is 24.2 kg/m^3 and increases steadily to 25.2 kg/m^3 until a depth of 30 meters, where it continues to increase at a slower rate. Sigma-t near the bed is 25.5 kg/m^3. In Fall 2001, sigma-t has a two layer structure ranging from 23.5 to 25 kg/m^3 with a pycnocline at a depth of 30-40 meters. The buoyancy frequency calculated from the record-mean sigma-t profiles is highest near the surface (~1 x 10^{-3} s^{-2}) in Spring. In the Fall, there is a higher buoyancy frequency (~1 x 10^{-3} s^{-2}) at the depth of the pycnocline than at all other depths, where N^2 is less than 0.25 x 10^{-3} s^{-2}.

B. Tidal Fluctuations in Stratification Profiles

Tidal-frequency fluctuations in sigma-t are prominent in both Spring and Fall 2001 (Figures 12 and 13) and are dominantly responsible for the density anomaly standard deviation (Figure 14). In the Spring, sigma-t variations reach a maximum of about 0.9 kg/m^3 between 10-20 meters depth and are minimal near-bottom. In the Fall, fluctuations are similarly large at all depths and reach their maximum at near the bottom.

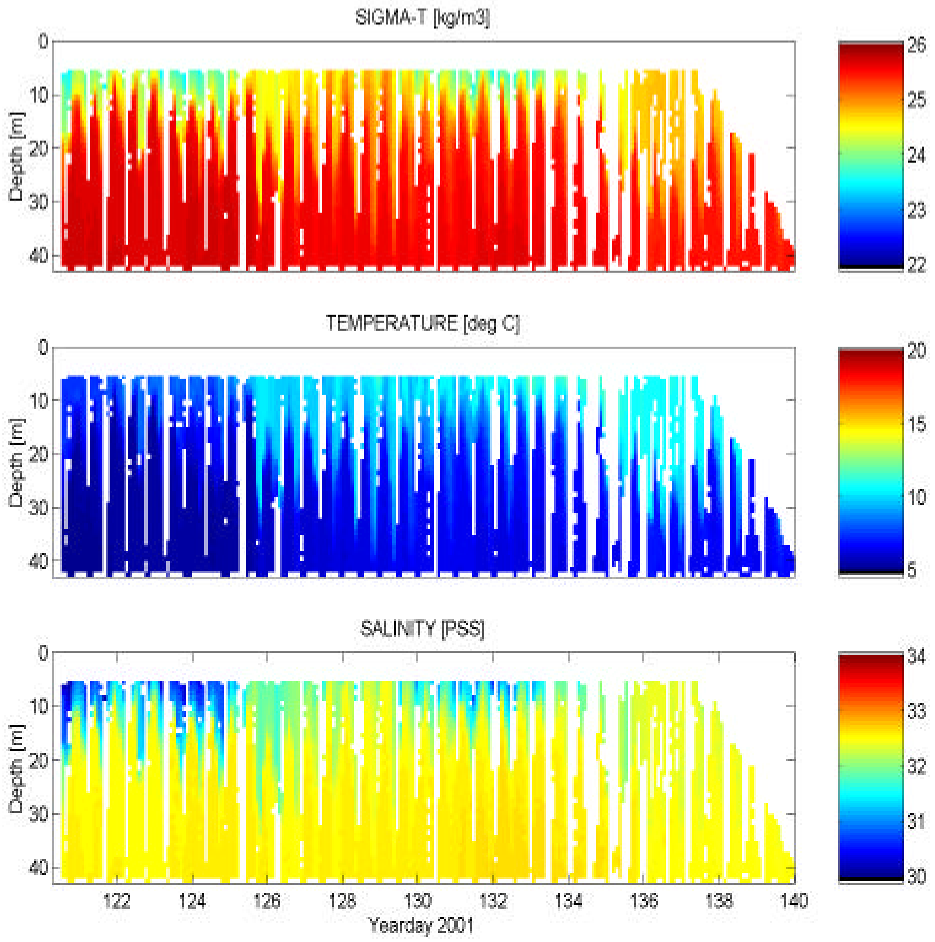

Figure 12. Spring 2001 Moored CTD Profiler Time-series Sigma-t is shown in the top plot, Temperature in the middle and Salinity in the lower plot. White patches are missing data.

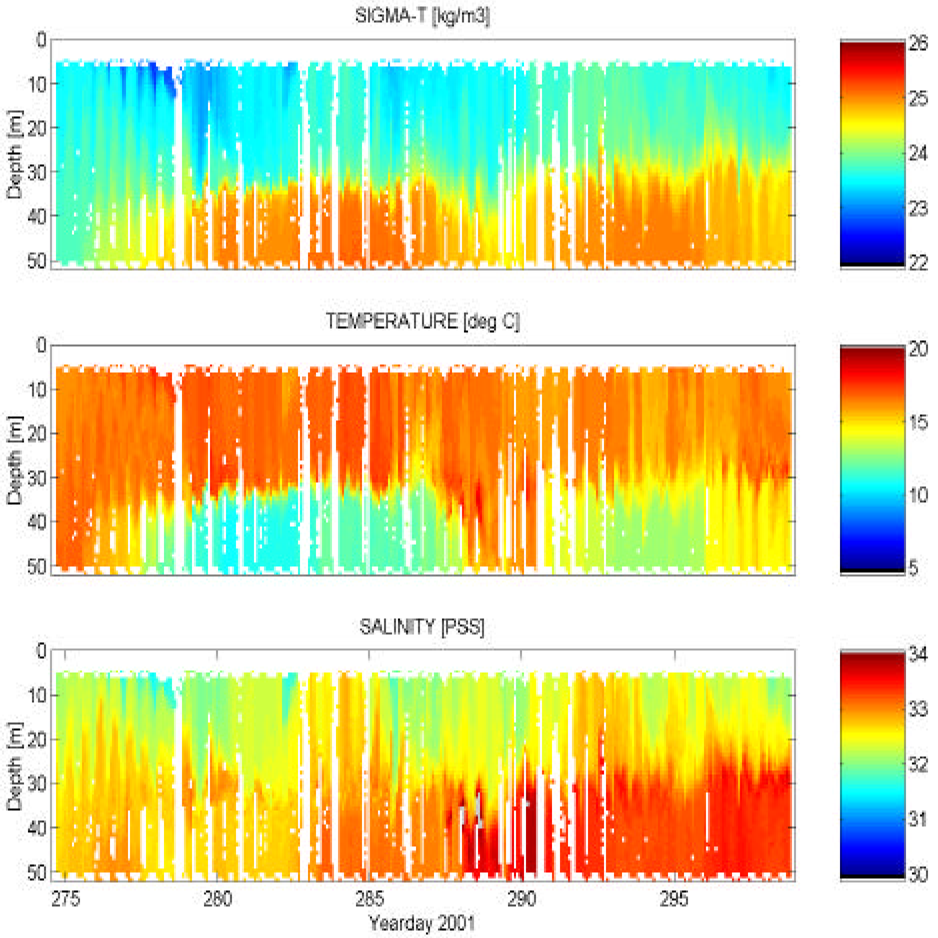

Figure 13. Fall 2001 Moored CTD Profiler Time-series As in Figure 12 (same colorbars) but Fall 2001 deployment. A sharp thermocline occurs at 35 meters depth.

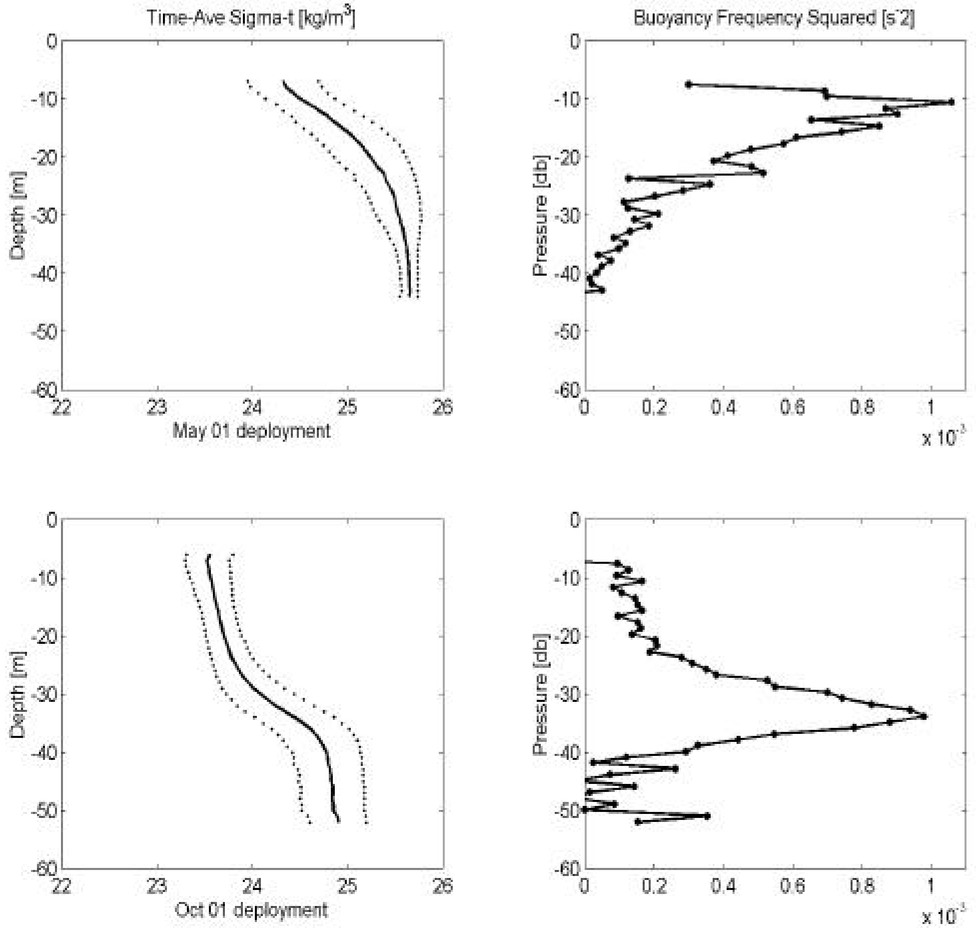

Figure 14. Record-mean Sigma-t and Buoyancy Frequency Squared Profiles Record-mean hydrographic profiles for Spring 2001 (upper) and Fall 2001 (lower). Sigma-t with standard deviation (left) and buoyancy frequency squared (right).

C. Mechanisms to Account for Tidal Fluctuations

The tidal fluctuations in density could be driven by a number of mechanisms. Two mechanisms that are commonly observed in coastal regions are horizontal advection of a front by tidal currents, and vertical velocities associated with enhanced internal tides. The first of these could account for the observed sigma-t fluctuations with a background horizontal density gradient and a horizontal current only (zero vertical velocity). In this mechanism, across-front velocity variations lead sigma-t variations by 90 degrees.

Internal tidal motion requires a vertical sigma-t gradient and a vertical velocity. Based on internal tide observations over continental shelves, a first baroclinic mode vertical structure is expected to be the most energetic; for this mode the vertical velocity has a maximum at mid-depth and the horizontal velocity has oppositely directed maxima near surface and bottom. For a propagating internal wave the phasing between sigma-t and the deep horizontal velocity in the direction of propagation is such that they are in phase and positively correlated. For a two layer internal wave idealization (e.g. Gill, 1982), values based on the top-to-bottom density difference and tidal sigma-t amplitudes for the study site include wavelengths of ~20 km, phase speeds of ~0.5 m/s, and typical horizontal velocities of ~10 cm/s.

The conservation of density equation used to investigate the mechanisms is

$$\frac{D\boldsymbol{r}}{Dt} = K_x \frac{\partial^2 \boldsymbol{r}}{\partial x^2} + K_y \frac{\partial^2 \boldsymbol{r}}{\partial y^2} + K_z \frac{\partial^2 \boldsymbol{r}}{\partial z^2} + So \qquad (8)$$

where *D/Dt* is the material derivative and *So* is a source term such as heating. In considering tidal fluctuations *So* is neglected. With the neglect of horizontal diffusive terms relative to the vertical one, the conservation equation can be rewritten as

$$\underset{\text{LRC}}{\frac{\partial \sigma_t}{\partial t}} = \underbrace{-u\frac{\partial \sigma_t}{\partial x} - v\frac{\partial \sigma_t}{\partial y}}_{\text{HA}} \underset{\text{VA}}{- w\frac{\partial \sigma_t}{\partial z}} \underset{\text{DIFF}}{+ K_z \frac{\partial^2 \sigma_t}{\partial z^2}} \tag{9}$$

where LRC represents the local rate of change term, HA the horizontal advection terms, VA the vertical advection term and DIFF the vertical diffusion term. For frontal advection, the balance will be between LRC and HA. For an internal tide, balance between LRC and VA is expected.

The moored CTD profiler deployments provide direct measurements for LRC of 2.2 x 10^{-5} kg/m^3/s, using 1 kg/m^3 sigma-t fluctuations (Figure 14) and the M_2 tidal period. The ADCP data offer typical values for *u* and *v* used in the calculation of HA of 30 cm/s. Towed-body hydrographic survey transects (Kirincich and Hebert, 2002) are used to estimate a value for the horizontal sigma-t gradient, which reaches 2.5 x 10^{-4} kg/m^3/m. Resulting HA values are nominally 7.5 x 10^{-5} kg/m^3/s.

If the balance was between LRC and VA, the vertical velocity required can be estimated as the ratio between LRC and $\partial\sigma/\partial z$. With an average vertical gradient of sigma-t in the Spring of 0.1 kg/m^3/m and 0.02 kg/m^3/m in the Fall, the vertical velocity value should be 0.022 cm/s in Spring and 0.06 cm/s in Fall. These values are much smaller than the nominal uncertainty of the measured ADCP vertical velocities.

Very coarse estimates of the magnitude of the DIFF term can be made with use of the optimal fit eddy viscosity values 1×10^{-3} m^2/s determined in Section V-B. By assuming eddy viscosity is equal to density diffusivity, such values of DIFF are smaller than HA though could be comparable in magnitude to LRC. However, the mechanism by which periodic increases and decreases in LRC would be matched by DIFF is not clear.

If a first baroclinic mode internal tide were responsible, horizontal velocities would tend to take on maximum values near surface and bottom, but in contrast, ADCP records reveal maximum values are reached at mid-depth. In addition, the fact that LRC is relatively large throughout the deeper nearly unstratified layer in Fall (lower left, Figure 14) runs counter to the idea that VA, instead of HA, balances LRC. In the absence of accurate vertical velocity data, however, the internal tide hypothesis can not be entirely discounted. If a front were not present at the site, an internal tide could possibly generate LRC because the required vertical velocities are small. However, based on the above estimates, it is concluded that the most likely balance is between LRC and HA, and therefore that the mechanism most responsible for causing the density fluctuations is horizontal advection of a front.

V. COMPARING OBSERVED NEAR-BOTTOM CURRENTS TO A FRICTIONAL ANALYTIC SOLUTION

Analytic solutions for the influence of friction on the vertical structure of tidal currents have been derived from the equations of motion (Prandle, 1982a; Maas and vanHaren, 1987; Visser, 1994). These solutions are for flat-bottom systems and are assessed here to see how well they can account for deep observations from the study site, where the bathymetry is complex. In this section, the behavior of an analytic solution is demonstrated using parameters appropriate to the study site, and an optimal fit of the analytic solution to the observations in the lower water column is made which yields values for the eddy viscosity and the linear bed stress coefficient.

A. The Analytic Solution

The system considered is a constant density, flat-bottom ocean with a constant vertical eddy viscosity and no horizontal eddy viscosity, under the influence of background rotation. The equations of motion defining the system in two dimensions, x and y, and the boundary conditions are

$$\frac{\partial u}{\partial t} - fv = -\frac{1}{\boldsymbol{r}_0}\frac{\partial p}{\partial x} + K\frac{\partial^2 u}{\partial z^2} \qquad (10)$$

$$\frac{\partial v}{\partial t} + fu = -\frac{1}{\boldsymbol{r}_0}\frac{\partial p}{\partial y} + K\frac{\partial^2 v}{\partial z^2} \qquad (11$$

$$\frac{\partial \bar{u}}{\partial z} = 0 \text{ at z =0} \tag{12}$$

$$\frac{\partial \bar{u}}{\partial z} = \frac{S}{H}\bar{u} = \frac{K_b}{K}\bar{u} \text{ at z = -H} \tag{13}$$

where *f* is the Coriolis parameter, *p* is pressure, $\boldsymbol{r}_0$ is the average density, *K* is a constant eddy viscosity, and *z* is the vertical coordinate, positive upward, z = -H is the depth at which the boundary condition is applied (the top of the bottom log layer taken to extend ~1 meter off the sea floor), and the constant bottom bed stress parameter $S = \frac{HK_b}{K}$ where K_b is a linear bed stress coefficient. The system is solved for time-periodic flow of the form shown in equation 3. The analytic solution (Prandle, 1982b; Maas and vanHaren, 1987; Visser, 1994) can be written

$$U^{\pm}(z) = U^{\pm}_{inv}\left(1 - \frac{\cosh\left(\boldsymbol{b}^{\pm}\frac{z}{H}\right)}{D^{\pm}}\right) \tag{14}$$

where $U^{\pm}$ are the complex amplitudes (see eq. 3), $U^{\pm}_{inv}$ is the inviscid response seen near the surface far from the influence of the frictional bottom boundary layer, and

$D^{\pm} = \frac{\boldsymbol{b}^{\pm}}{S}\sinh \boldsymbol{b}^{\pm} + \cosh \boldsymbol{b}^{\pm}$ where

$\beta^{\pm}$ = {(1+i)(H/δ^{+}) for ω+f >0
{(1-i)(H/δ^{+}) ω+f <0

$$\beta^{\pm} = \begin{cases} (1+i)(H/\delta^{-}) & \text{for } \omega\text{-}f > 0 \\ (1-i)(H/\delta^{-}) & \omega\text{-}f < 0 \end{cases}$$

with $\delta^{\pm} = +\sqrt{\frac{2K}{|w \pm f|}}$ a characteristic frictional boundary layer thickness for each rotating component (+ CCW, - CW in time).

The analytic solution changes as a function of eddy viscosity (K) and the linear bed stress coefficient (K_b) (Figure 15). Five combinations of eddy viscosity and linear bed stress have been used to portray the changing features of the analytic solution. All five calculations include currents with a surface A^+ of 5 cm/s and A^- of 10 cm/s, chosen to be representative of observed tidal currents (Section III). The values for f and w used in the analytic solution are those at the study site, 9.56×10^{-5} s^{-1} and 1.41×10^{-4} s^{-1}, respectively; the ratio of δ_- to δ_+ is 0.44.

As seen in the next subsection, central values for eddy viscosity (K), 5.0×10^{-3} m^2/s, and linear bed stress coefficient (K_b), 1×10^{-3} m/s, are representative of currents at the study site. The ellipses calculated for the central case (top row, Figure 15) decay in amplitude with depth, show inclination that decreases then slightly increases with depth, and have a phase advance with depth of about 40°. The influence of friction δ_+ is concentrated in the lower ten meters while δ_- is in the lower 15 meters. The other four calculations include the following values: "low-K", 5.0×10^{-4} m^2/s, "high-K", 5.0×10^{-2} m^2/s, "low-K_b", 1×10^{-4} m/s, and "high-K_b", 1×10^{-2} m/s. The low-K and central-K_b case (second row, Figure 15) indicates that the heights of frictional influence, $\delta_\pm$, are lowered to the deepest ten meters. The high-K and central-K_b case (third row, Figure 15) shows an increase in the frictional influence such that it extends throughout most of the water column for δ_+ and the entire water column for δ_-, causing a majority of the ellipse parameters to change uniformly with depth but by small amounts. For example, the phase changes by only 2^o.

The influence of friction, $\delta_\pm$, in the central-K and low-K_b case (fourth row, Figure 15) is ~10-15 meters deeper than in the high-K and central-K_b case, and weak changes in inclination occur in opposite directions for the two cases. However, other attributes between the two are similar. Finally the central-K and high-K_b case (last row, Figure 15) has semi-major and semi-minor axes similar to the central case, with the same scales for $\delta_\pm$; the largest difference lies in the steepness of the parameters within the bottom boundary layer near $z = -H$. This final case demonstrates that current ellipse characteristics of the analytic solution are relatively insensitive to large values of bed-stress coefficient.

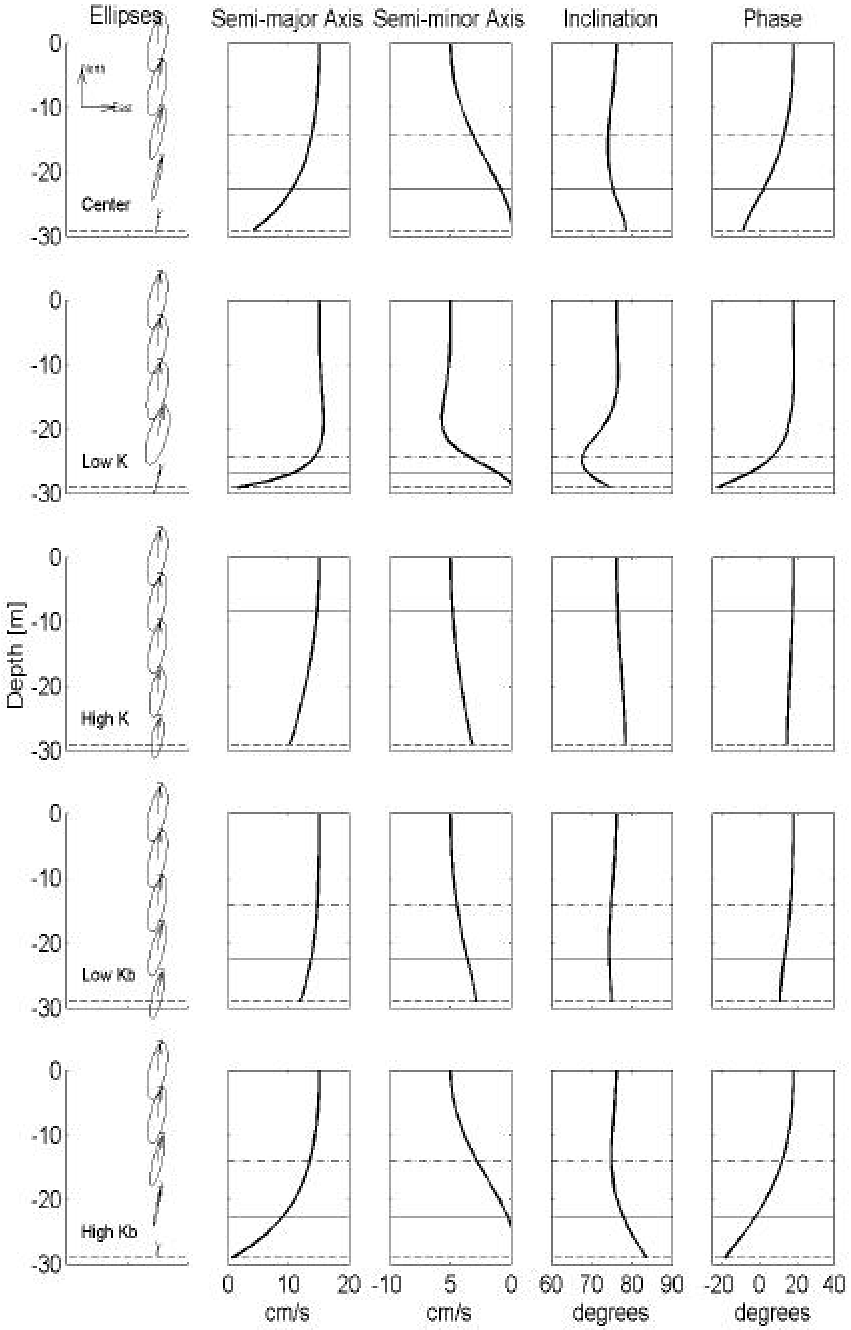

Figure 15. Analytic Solution Ellipses and their parameters for different combinations of eddy viscosity and linear bed stress. Top row: K = 5 x 10^{-3} m^2/s and K_b = 1 x 10^{-3} m/s; Second row: K = 5 x 10^{-4} m^2/s and K_b = = 1 x 10^{-3} m/s; Third row: K = 5 x 10^{-2} m^2/s K_b = 1 x 10^{-3} m/s; Fourth row: K = 5 x 10^{-3} m^2/s and K_b = 1 x 10^{-4} m/s ; Fifth row: K = 5 x 10^{-3} m^2/s and K_b = 1 x 10^{-2} m/s. Horizontal lines are δ_- (dash-dot), δ_+ (solid), and top of bottom log layer, H_{ll} above seafloor (dashed).

B. Optimal Fit

Optimal fits between the measured currents and the analytic solution (referred to as "the model") were determined in the near bottom portion of the water column, returning best-fit values for eddy viscosity (K) and the linear bed stress coefficient (K_b). The model is expected to account for the vertical structure of measurements near the bottom only. Therefore the fit is made using only data deeper than an arbitrary depth, z_{fit}, shallower than bottom boundary frictional effects, where the analytic solution is expected to asymptote to its shallow limit; the model and data are required to match at a depth of z_{fit}.

To perform the optimal fit, the Nelder-Mead downhill simplex method (Nelder and Mead, 1965; Press et al, 1992; Mathews and Fink, 1999) was implemented. The method is used for nonlinear minimization of a cost function (CF) defined as

$$CF = \sum_{i=1}^{M} \left[\left(U_d^+(z_i) - U_m^+(z_i) \right)^2 + \left(U_d^-(z_i) - U_m^-(z_i) \right)^2 \right] \tag{15}$$

where there are M ADCP bins deeper than z_{fit}, and $U_d^{\pm}$ and $U_m^{\pm}$ are counter-clockwise and clockwise data (*d,* calculated as in eq. 3) and model (*m,* calculated as in eq. 14) points. In this method, in N dimensions a simplex is defined as a figure consisting of N+1 vertices. In the case of K and K_b (two dimensions), the simplex is a triangle. The optimization starts at specified initial values and travels downhill towards lower values of the function, contracting and expanding the simplex along the way.

To initialize the optimization, starting values of K and K_b at each site were chosen by an initial visual inspection. The North, West, Central, East and South sites have a z_{fit} of 7, 20, 25, 30 and 30 meters from the surface, respectively. The extent of the bottom log layer (H_{ll}) off the bottom is taken to be 1 meter.

For most records, the optimal-fit solution matches the observations at all depths extremely well (for example, Figure 16 upper), with the solution lying well within the confidence intervals of measured ellipse parameters. For some records, particularly in Spring, the optimal-fit solution captures the frictional effects adequately near the bed, but as expected is unable to represent the observations near the surface (for example, Figure 16 lower) where influences other than friction are likely to be important (see Section III-D).

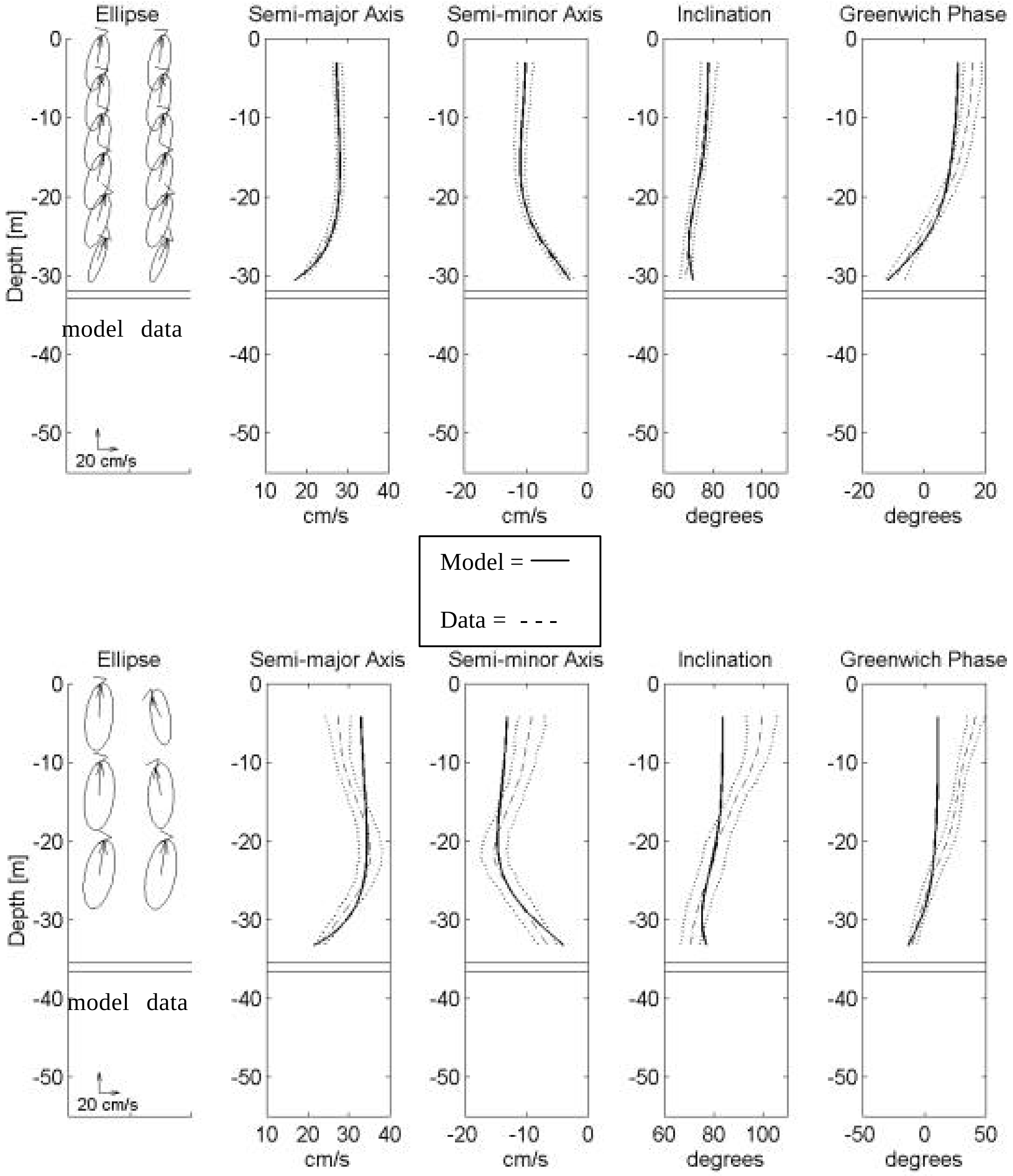

Figure 16. Model Fit to the Observations Fall 2001 West site (upper) and Spring 2002 Central site (lower) ellipses (left) and parameters (right) for the model (solid line) and data (dash-dot lines with 95% confidence intervals). Two horizontal lines in each frame indicate depth of application of bottom boundary layer and water depth.

The majority of the sites have optimal values of linear bed stress (K_b) between 2.5 x 10^{-4} and 1.15 x 10^{-3} m/s and eddy viscosities (K) of 0.001 to 0.003 m^2/s (Figure 17). To test the sensitivity of these values with respect to z_{fit}, 2 meters were added and subtracted from the original z_{fit} at each site and the optimization recalculated. The resulting variation of K_b was between 0.0001 and 0.001 m/s and of K by about 0.002 m^2/s. In some cases (e.g. Fall 2001 East), changes to z_{fit} resulted in non-convergence of the optimization. To test sensitivity of values to the bottom log layer thickness (H_{ll}), it was changed from 1 meter to 0.5 and 2 meters. This changed K_b by at most 0.001 m/s and K by at most 0.004 m^2/s. The aggregate RMS uncertainty to changes in z_{fit} and H_{ll} is 0.75 x 10^{-3} m/s in the Kb direction and 2 x 10^{-3} m^2/s in the K direction. Optimal values for all seasons and depths differ from each other by amounts comparable to this uncertainty. No strong trend in optimal K and K_b values with season or water depth is apparent.

Despite its omission of the effects of stratification and bathymetric variations which are substantial at the study site, the analytic solution accounts for the observed vertical structure of deep tidal currents very well.

A value for the drag coefficient C_d can be calculated using an energy criterion $K_b = 8/3\pi \times C_d U(0)$ where U(0) is the tidal current amplitude at the bottom. Using the optimal-fit linear bed stress coefficient (K_b = 2.5 x 10^{-4} to 7.5 x 10^{-4} m/s) a drag coefficient of C_d = 1.4 x 10^{-3} to 4.4 x 10^{-3} is determined. These values agree with previous studies (e.g., 2-4 x 10^{-3} of Maas and Van Haren, 1987).

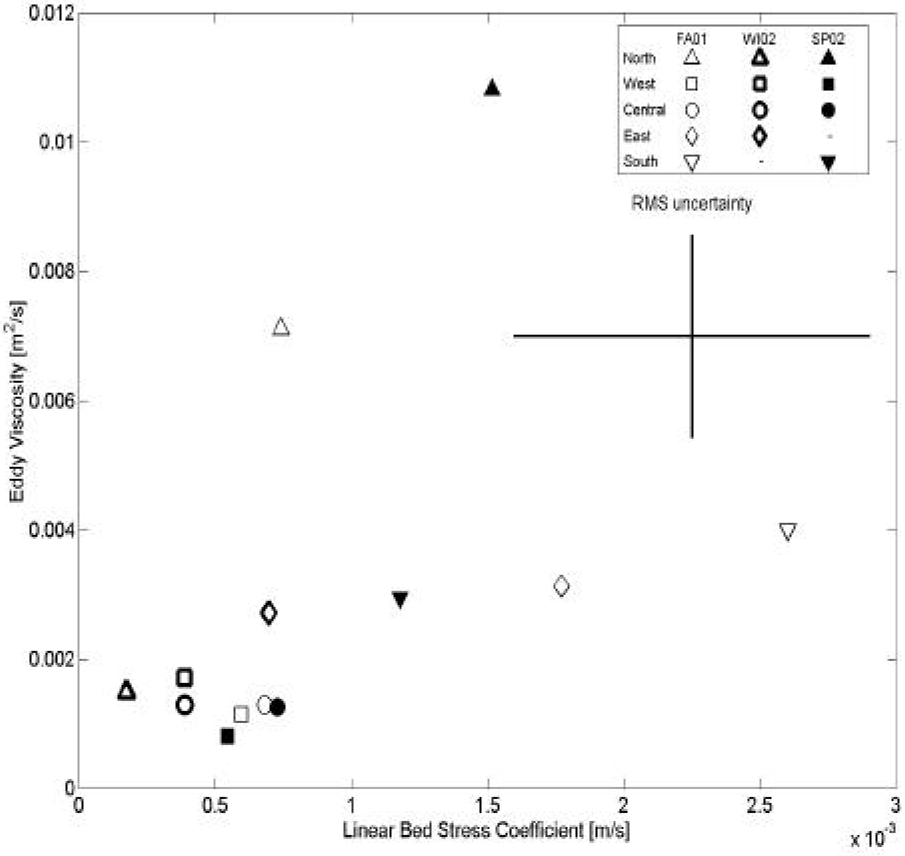

Figure 17. Optimal Eddy Viscosities and Stress Coefficients Linear Bed Stress Coefficient is the x-axis and eddy viscosity is the y axis. Triangles, squares, circles, diamonds, and upside-down triangles indicate North, West, Central, East, and South sites during Fall 2001 (open), Winter 2002 (bold), and Spring 2002 (filled).

Optimal eddy viscosity values of 2 x 10^{-3} m^2/s, calculated here, are not inconsistent with experimental values in the North Sea of 1.4 x 10^{-3} m^2/s (Maas and vanHaren, 1987) and those for the Dover Straits 2.5 x 10^{-3} m^2/s (Prandle, 1982a). Values of eddy viscosity as high as 1 x 10^{-2} m^2/s and 0.1 m^2/s have been reported for the Rhine region (Souza and Simpson, 1996) and the Celtic Sea (Soulsby, 1990), respectively.

The optimal-fit eddy viscosities are generally in agreement with values determined by microstructure measurements (10^{-3} m^2/s; Levine et al., 2002) from the same site. The optimal-fit method used here determines an eddy viscosity value that must be considered an average across at least one tidal cycle and across the deepest several 10s of meters. In contrast, most microstructure turbulence measurements apply for less than a tidal cycle and at a more limited range of depths.

The calculated values of optimal eddy viscosity for this site (10^{-3} m^2/s) are not inconsistent with those predicted by the MIT General Circulation Model applied to the FRONT site (Edwards, pers. comm, 2002). The model parameterizes vertical mixing using the KPP algorithm of Large et al. (1994). Values predicted by the model are as large as 10^{-2} m^2/s in places. However, in the model the viscosity is highly variable both in space and time.

Finally, in order for the model to potentially account for the observations better in the upper water column, the optimization could be performed using a weighting function with depth that is more sophisticated than the present step-function. Eddy viscosity could also be a function of depth with numerical solutions used to solve the system. Neither of these two approaches seems warranted given the goodness of fit already achieved in the lower water column.

VI. Description of ADCP Time-series During a CTD Deployment

While previous sections used current meter records spanning more than 2 spring-neap cycles, in this section time-series fluctuations on shorter time periods are examined. The aim is to describe such fluctuations and determine the extent to which they are related to the spring-neap cycle, wind events, sub-tidal flow, or changes in stratification.

Harmonic fits of ADCP currents to the M_2 tidal period were performed on sequential two-day intervals, each offset by 36 hours from the previous, for the duration of the record. Errors associated with this method are higher and more variable than with the record-mean analysis. Two records were examined, the SP01-C deployment (see Table 1) and the Fall 2001 South deployment, from locations about 1 km apart, because both sites had concurrent CTD deployments for a month (Section IV). Sub-tidal currents were calculated by application of a 25-hour half-width low-pass filter.

A. Spring-Neap Cycles

The Spring and Fall time fluctuations of the current amplitudes (L_{maj} and L_{min}) are consistent with the spring/neap cycle. During spring tides, the semi major axis in Spring (Figure 18) and Fall (Figure 19) is double that during neap tides. During both seasons, the semi-major axis reaches 35-45 cm/s at 15-20 meters depth during spring tides and is nearly uniform with depth at 10-20 cm/s during neap tides.

The semi-minor axis becomes two times as negative during times of spring tide than that of neap. No spring-neap variations in ellipse inclination, phase or eccentricity are prominent for either deployment.

B. Counter-rotating Shallow and Deep Tidal Currents

Tidal currents that rotate oppositely in time at shallow and deeper depths in association with stratification are seen intermittently. Souza and Simpson (1996) observed eccentricity of opposite sign in the upper water column in the Rhine when strong stratification across a mid-depth interface existed. In the present analysis there is a suggestion that similar flow structure is occurring, if intermittently, during the early portion of the Fall deployment (Figure 19). The stratification at this time is most similar in structure to the two-layer form studied by Souza and Simpson. This pattern does not persist throughout the entire record so it is not apparent in the record-mean analysis of Section III. The different patterns of the present study site and that of Souza and Simpson is most likely due to the position of the present study site at the mouth of a large estuary system, and the associated different strength of tidal currents.

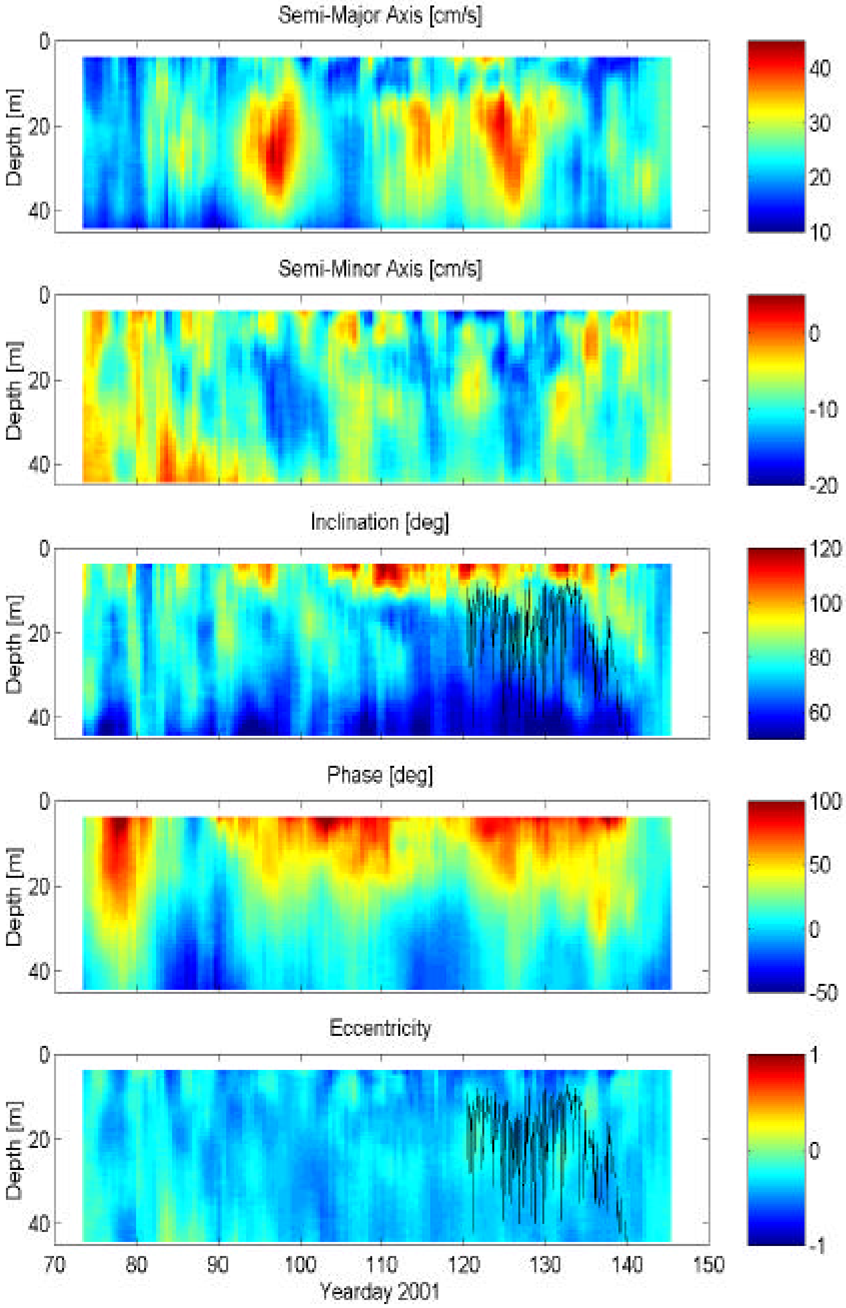

Figure 18. Tidal Ellipse Parameters and Auxiliary Information for the Spring 2001 site M_2 ellipse parameters (black lines on inclination and eddy viscosity indicate depth of maximum N^2 value), the low-pass East and North velocities, sigma-t profiles, winds and tidal heights from Montauk Point, optimal eddy viscosity and linear bed stress coefficient. Figure spans two pages.

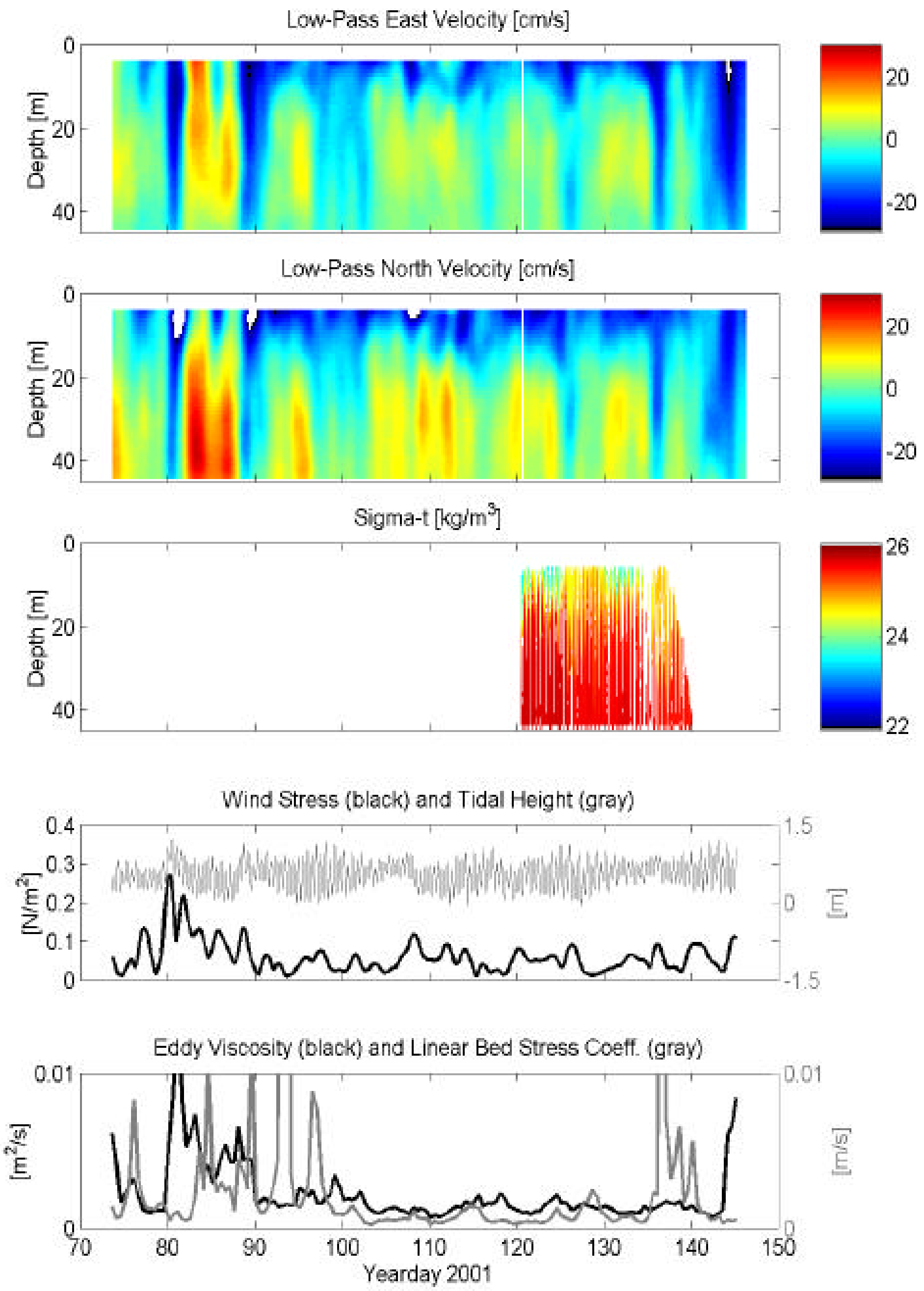

Figure 18. cont.

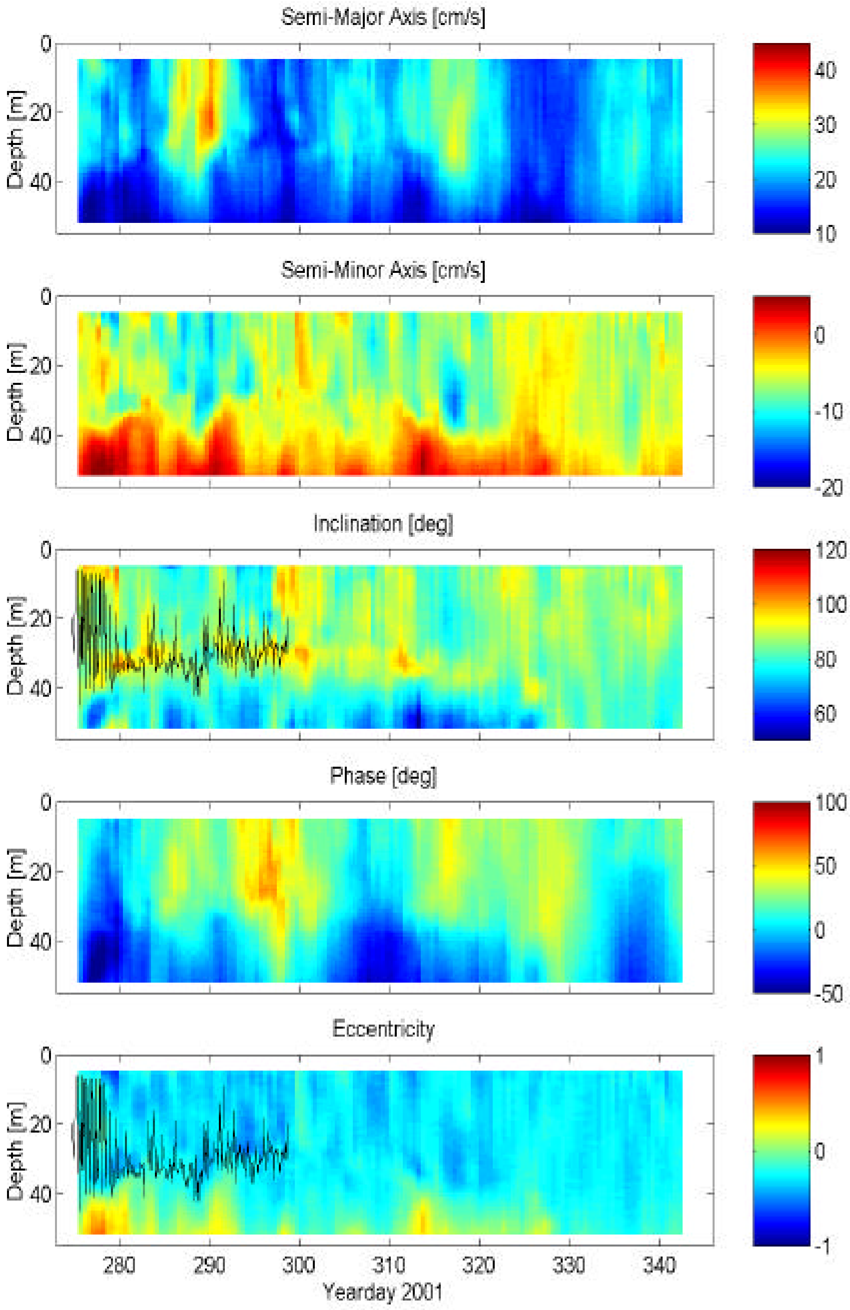

Figure 19. Tidal Ellipse Parameters and Auxiliary Information for the Fall 2001 site As in Figure 18, but for the Fall 2001 record. Figure spans two pages.

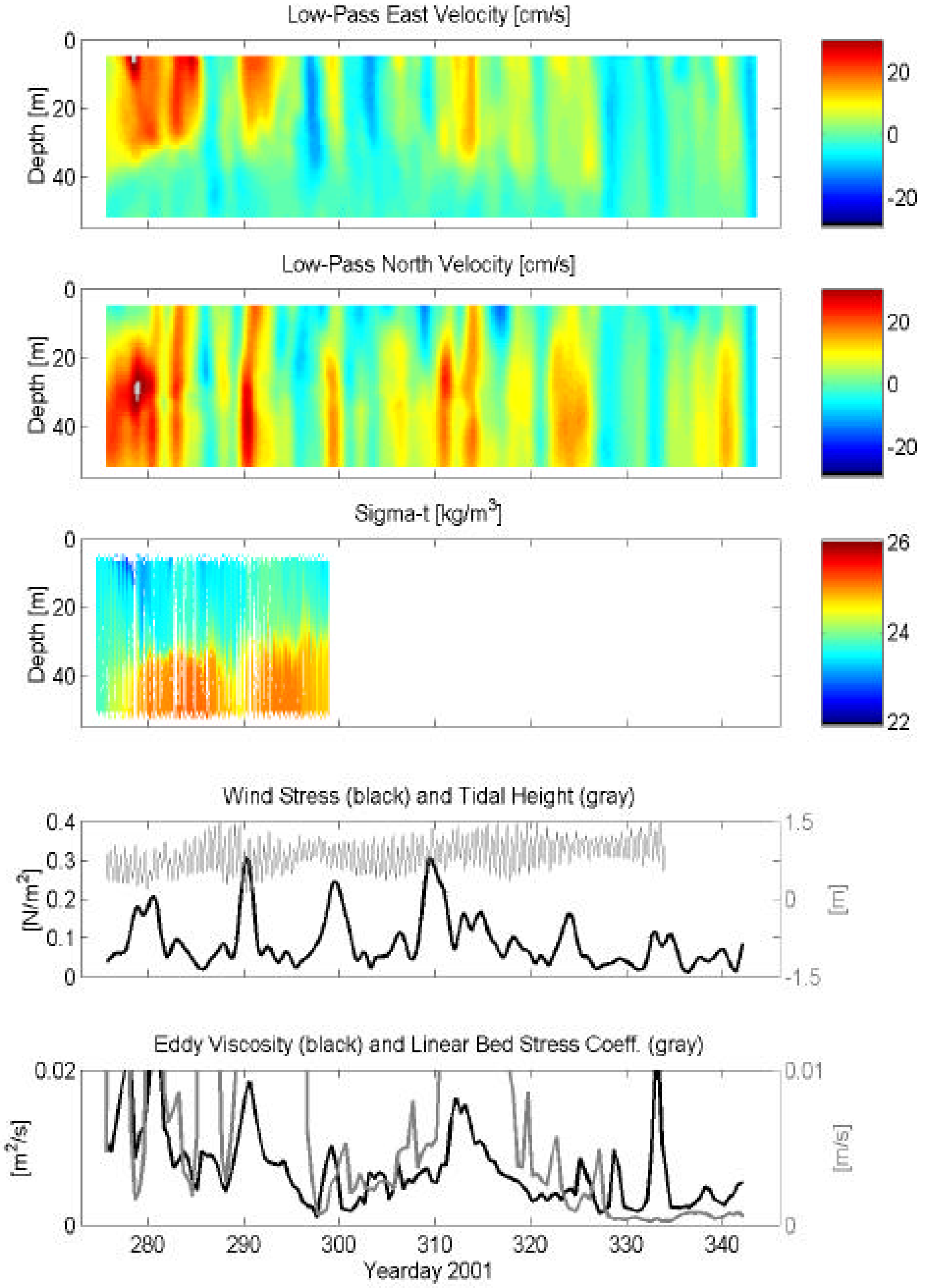

Figure 19. cont.

C. Ellipse Inclination and Stratification

In both seasons there is a noticeable relationship between inclination and stratification at the depth of the pycnocline, 10 meters in Spring and 35 meters in Fall, that is not observed in the other ellipse parameters. The vertical profile of inclination takes a local maximum in Fall near the depth at which N^2 is maximal. In the absence of CTD profiles, the depth of the maximum stratification can during some parts of the record still be apparent in viewing inclination data (see Figure 19, after yearday 300). This suggests the possibility that inclination could be used, in the absence of CTD profiles as is commonly the situation, as a proxy to assess the presence or absence of a pycnocline and to determine its depth.

D. Sub-tidal Currents

Low-passed currents are maximal near the surface during Spring. The relationship between this seasonal shift and current ellipses has been described in Section III-D. In both seasons, low-passed currents vary intermittently in time by about 20 cm/s. During certain intervals of the record, fluctuations in the semi-minor axis (and thus eccentricity) seem related to low-passed currents. However, a clear pattern in this relationship is not apparent.

E. Optimal Linear Bed Stress Coefficient and Eddy Viscosity

Optimal linear bed stress coefficient and eddy viscosity values of the analytic solution were calculated for the time series data in the same manner as stated above and with a few exceptions converged without difficulty. High optimal values of K_b are determined by the optimal fit for some time periods. The overall structure of the tidal ellipses is relatively insensitive to high K_b values (see Figure 15 fifth row). The linear bed stress coefficient in the Spring is 0.0012 ± 0.0013 m/s and 0.0038 ± 0.0028 m/s in the Fall.

The mean values computed for the eddy viscosity during Spring are 0.002 ± 0.001 m^2/s whereas values are higher, 0.007 ± 0.002 m^2/s, in the Fall. While the 2-day interval analysis of this section suggests a seasonal difference in eddy viscosity, the above analysis based on records spanning multiple spring-neap cycles (Section V-B) did not determine a clear seasonal difference in the parameter. However, larger uncertainties associated with the present calculation are comparable to the seasonal difference.

There exist a few 1-2 day periods when the optimal-fit eddy viscosity increases substantially to values greater than 0.015 m^2/s. There is no evident relationship between these events and the spring/neap cycle, nor to changes in stratification, rather they are associated with peak wind stress levels. In Spring, at yearday 80, a wind event causes stresses to rise from 0.05 to 0.25 N/m^2, and within a day the eddy viscosity increases from 0.008 to 0.016 m^2/s. In the Fall, at yeardays 280, 290, 299, and 309, the wind stress is elevated to 0.2 - 0.3 N/m^2 and at days 324 and 333 the stress is also slightly elevated. An increase in eddy viscosity occurs between half a day to a whole day after each of these wind events. This response could be due to wind mixing extending deeper into the water column and increasing eddy viscosity, or it could be a wind-driven mean flow that increased the bottom boundary layer thickness and therefore bottom boundary layer eddy viscosity values.

Fluctuations in linear bed stress and eddy viscosity may be associated with the absence of a time-varying mean bottom stress coefficient in the bottom boundary condition of the analytic solution. The time-varying mean bottom stress term could be incorporated in the analytic solution for the vertical structure of tidal currents. This term may offset the fluctuations calculated by the optimal fit here, causing both the eddy viscosity term and linear bed stress term to possibly be constant in time.

VII. SUMMARY

Observed attributes of tidal currents and hydrographic profiles on the continental shelf at the mouth of Long Island Sound (Figure 1a) are described and interpreted. The site is characterized by complicated bathymetry, hydrography strongly influenced by relatively fresh outflow (Figure 2) from the LIS/BIS estuarine systems, and numerous fronts as observed by satellite. ADCP records are from Fall 2001, Winter 2002 and Spring 2002 in a 5-pt cross central array 10 km across in water depths of 20-70 m, and three far-field sites (Figure 1b). They enable assessment of the energy partition among non-tidal and tidal constituents, spatial gradients in tidal currents including weakening with distance offshore, and comparison of near-bottom currents to a frictional analytic solution at high vertical resolution. Time-series of density profiles from moored CTD profilers resolve prominent tidal fluctuations and facilitate investigation of responsible mechanisms.

Tidal currents account for 47-95% of the total kinetic energy in the central array, with higher values seen in shallower water (Figure 4, pies). The five most energetic tidal constituents are M_2, S_2, O_1, N_2, and K_1, with M_2 accounting for roughly 85% of the tidal energy and the other four tidal constituents contributing less than 10% each to the kinetic energy (Figure 4, bars). At the far-field sites, 25-35% of the energy is tidal, and M_2 accounts for 75-82%. These patterns are the consequence of near resonance of the LIS system with the M_2 constituent, which is the focus of the remainder of the study.

Horizontal structure of tidal currents is seen in tidal ellipses of vertical mean currents (Figure 5) with major axes oriented towards the mouth of the Block Island Sound, a direction that is consistent with exchange between Block Island Sound and the continental shelf. The orientation indicates that the influence of the complex bathymetry is minimal. Tidal current amplitude decreases offshore from 55 cm/s to 20 cm/s across the 10-km span of the central array. Weaker amplitudes (~8 cm/s) are seen at the far-field sites: ellipses to the south of Long Island are directed along the shore; off Block Island, ellipses are directed to the East of the island and the instantaneous velocity reveals a phase advance relative to the central array; at the deeper offshore site ellipses are nearly circular in shape.

Vertical structure of tidal currents during all three seasons (Figures 6, 7, and 8) have several common characteristics, particularly in the deepest 10-25 m. Velocity vectors rotate clockwise in time throughout the water column. In the deepest 5-15 meters, as the bottom is approached there is a decrease in current amplitude by about 10-15 cm/s, ellipse inclination (Figure 3) decreases by 20-50º, and there is a phase advance in the range of 10-50º, indicating that the time of maximum current near the bed precedes that near the surface. At the deeper offshore site the ellipses have very little vertical structure which is attributed to the lessened frictional influence associated with lower amplitudes there.

Differences in the vertical structure of tidal currents between seasons occur, mostly in the upper water column. In Fall 2001 the current amplitude is relatively uniform except near the bottom. In contrast, during Spring 2002, a more-pronounced mid-depth maximum in current amplitude occurs (Figure 8). In Spring, tidal current ellipses in the shallowest ~10 m are notably smaller and changed in orientation by roughly 90 degrees (Figure 12). These differences appear to be associated with enhanced shallow buoyant outflow from Long Island Sound in springtime as well as seasonal changes in stratification profiles.

Moored CTD profiler data collected for a one-month period in Spring 2001 and another in Fall 2001 at the southern edge of the central array (Figure 1) in ~50 m of water reveal similar top-to-bottom density differences (Figures 12 and 13). Both temperature and salinity stabilize the density. However, in the Fall the record-mean density profile has a two layer structure with a sharp pycnocline at a depth of 30-40 meters, while the Spring profile includes a continuous density gradient in the shallowest ~20 m overlying a deep layer of relatively constant density (Figure 14).

Tidal fluctuations in density are prominent in the moored CTD profiler records from both Spring and Fall 2001 and could be due to the horizontal advection of a front, or the presence of internal tides. Estimates of terms in the density conservation equation are made using the moored CTD profiler records, ADCP currents, and horizontal gradients in hydrography from towed-body surveys. Results indicate that horizontal advection of a front is most responsible for tidal density fluctuations.

The extent to which an analytic solution (eq. 14, Prandle, 1982a; Maas and vanHaren, 1987; Visser, 1994) for a flat-bottom, constant eddy viscosity ocean can account for observed near-bottom current characteristics (listed above) is assessed. The solution does very well despite its omission of stratification and bathymetric effects known to be substantial at the site. Surface observations differ significantly from the analytic solution in the Spring, as expected because processes other than friction are important at these shallow depths. Eddy viscosities determined by an optimal-fit are between 0.001 and 0.003 m^2/s, and linear bed stress coefficients are between 2.5×10^{-4} and 1.15×10^{-3} m/s and do not reveal systematic dependence on season or water depth. These values are consistent with microstructure measurements from the site as well as those produced by numerical models used in the region.

Sub-tidal fluctuations of tidal current ellipses and parameters were investigated using a harmonic fit of the ADCP currents to the M_2 tidal period on two-day intervals, each offset by 36 hours from the previous, for the duration of the record. The Spring and Fall time fluctuations (Figures 18 and 19) of the current amplitudes are consistent with the spring/neap cycle. During intermittent time periods, ellipses are traced counter-clockwise deeper than the pycnocline, which is similar to the observed patterns in tidal currents attributed to the influence of stratification in other coastal regions. Mid-depth maximum values of ellipse inclination angle appear to be associated with pycnocline stratification. An obvious relationship between the low-passed currents and the ellipse parameters is not present. Values of eddy viscosity from optimal fits to the analytic solution peak during major wind events, and are weakly affected by stratification, suggesting the effects of wind are felt throughout the water column; a wind-driven low-frequency current that increases the bottom boundary layer thickness could also be responsible. Fluctuations in eddy viscosity and linear bed stress may also be associated with the absence of a time-varying, mean bottom stress coefficient in the bottom boundary conditions of the analytic solution.

REFERENCES

Bruno, M., R. Mananes, J.J. Alonso, A. Izquierdo, L. Tejedor, and B.A. Kagan. (2000). Vertical structure of the semidiurnal tidal currents at Camarinal Sill, the strait of Gibraltar. *Oceanologica Acta.*, 23 (1), 15-24.

Codiga, D.L., J.A. Rice, and P.S. Bogden. (2000). Real-time delivery of subsurface coastal circulation measurements from distributed instruments using networked acoustic modems. Proc. MTS/IEEE Oceans 2000. Vol 1, pp 575-582.

Codiga, D.L., and A.E. Houk. (2002). Current profile timeseries from the FRONT moored array. Technical Report. The University of Connecticut.

Davies, A.M. (1992). Modelling currents in highly sheared surface and bed boundary layers. *Continental Shelf Research*, 12,189-211.

DiMarco, S.F., and R.O. Reid. (1998). Characterization of the principal tidal current constituents on the Texas-Louisiana shelf. *Journal of Geophysical Research,* 103, 3093-3109.

Gill, A.E. (1982). Atmosphere-Ocean Dynamics, Academic Press, New York. pp. 662.

Godin, G. (1972). The analysis of tides. University of Toronto Press, Toronto.

Kirincich, A., and D. Hebert. (2002). NOPP Front Resolving Observational Network with Telemetry (FRONT) Project: Frontal scale hydrographic surveys. GSO Technical Report No. 2002-01.

Knauss, J.A. (1997). Introduction to Physical Oceanography. 2nd ed. Prentice Hall, Upper Saddle River, New Jersey.

Kundu, P, J.O. Blanton, and M.M. Janopaul. (1981). Analysis of current observations on the Georgia Shelf. *Journal of Physical Oceanography*, 11, 1139-1149.

Large, W. G. and S. Pond. (1981).Open ocean momentum flux measurements in moderate to strong winds. *Journal of Physical Oceanography*, 11, 324-336.

Large, W. G., J.C. McWilliams and S.C. Doney. (1994). Oceanic vertical mixing: A review and a model with a nonlocal boundary layer parameterization. *Reviews of Geophysics*, 32, 363-403.

Levine, E.R., L. Goodman, R.G. Lueck, and C.A. Edwards. (2002). Turbulent budgets and model/data comparison for AUV-based sampling in the FRONT coastal front. *Eos, Transactions, AGU* , 83(4), Ocean Sciences Meet. Suppl., Abstract OS41N-10.

Maas, L.R.M., and J.J.M. van Haren. (1987). Observations on the vertical structure of tidal and inertial currents in the central North Sea. *Journal of Marine Research*, 45, 293-318.

Mathews, J.H. and K.D. Fink. (1999). Numerical methods using MATLAB. Prentice Hall, Upper Saddle River, New Jersey.

Nelder, J.A. and R. Mead. (1965). A simplex method for function minimization. *Computer Journal*, 7, 308-313.

Pawlowicz, R., B. Beardsley, and S. Lentz. (2002). Classical tidal harmonic analysis including error estimates in MATLAB using T_Tide. *Computers and Geosciences*, 28 (8), 929-937.

Prandle, D. (1982a). The vertical structure of tidal currents and other oscillatory flows. *Continental Shelf Research*, 1, 191-207.

Prandle, D. (1982b). The vertical structure of tidal currents. *Geophysical and Astrophysical Fluid Dynamics*, 22, 29-49.

Press, W.H., B.P. Flannery, S.A. Teukolsky, and W.T. Vetterling. (1992). Numerical recipes in C: The art of scientific computing. 2nd ed. Cambridge University Press, New York.

RD Instruments. (1998). Workhorse technical manual. San Diego. pp 222.

Soulsby, R.L. (1990). Tidal-current boundary layers. *In*: Le Mehaute, B., Hanes, D.M (eds.), The Sea, vol. 9A, Ocean Engineering Science, pp 523-566. Wiley-Interscience, New York.

Souza, A.J., and J.H. Simpson. (1996). The modification of tidal ellipses by stratification in the Rhine ROFI. *Continental Shelf Research,* 16 (8), 997-1007.

Tang, C.L. and D.J. Belliveau. (1994). Vertical structure of currents on the Northern Grand Bank - a view from a bottom mounted Acoustic Doppler Current Profiler. *Continental Shelf Research*, 14 (12), 1331-1347.

Teague, W.J., H.T. Perkins, G.A Jacobs, J.W. Book. (2001). Tide observations in the Korea-Tsushima Strait. *Continental Shelf Research*, 21, 545-561.

Tsimplis, M.N. (2000). Vertical structure of tidal currents over the Camarinal Sill at the Strait of Gibraltar. *Journal of Geophysical Research,* 105, 19,709-19,728.

Valle-Levinson, A., C. Li, T.C. Royer, and L.P. Atkinson. (1998). Flow patterns at the Chesapeake Bay entrance. *Continental Shelf Research*, 18, 1157-1177.

Visser, A.W., A.J. Souza, K. Hessner and J.H. Simpson. (1994). The effect of stratification on tidal current profiles in a region of freshwater influence. *Oceanologica Acta*, 17 (4), 369-381.